nature communications

Article

https://doi.org/10.1038/s41467-025-57770-1

Responsive DNA artificial cells for contact and behavior regulation of mammalian cells

Received: 23 July 2024

Accepted: 4 March 2025

Published online: 11 March 2025

Check for updates

Miao Wang[1,2,3,4], Hexin Nan[1,3], Meixia Wang[1,2], Sihui Yang[1,3], Lin Liu[1,3], Hong-Hui Wang[1,2,5] ✉ & Zhou Nie[1,3,5] ✉

Artificial cells have emerged as synthetic entities designed to mimic the functionalities of natural cells, but their interactive ability with mammalian cells remains challenging. Herein, we develop a generalizable and modular strategy to engineer DNA-empowered stimulable artificial cells designated to regulate mammalian cells (STARM) via synthetic contact-dependent communication. Constructed through temperature-controlled DNA self-assembly involving liquid-liquid phase separation (LLPS), STARMs feature organized all-DNA cytoplasm-mimic and membrane-mimic compartments. These compartments can integrate functional nucleic acid (FNA) modules and light-responsive gold nanorods (AuNRs) to establish a programmable sense-and-respond mechanism to specific stimuli, such as light or ions, orchestrating diverse biological functions, including tissue formation and cellular signaling. By combining two designer STARMs into a dual-channel system, we achieve orthogonally regulated cellular signaling in multicellular communities. Ultimately, the in vivo therapeutic efficacy of STARM in light-guided muscle regeneration in living animals demonstrates the promising potential of smart artificial cells in regenerative medicine.

Artificial cells are synthetic systems engineered to emulate the dynamic and life-like capabilities of natural cells[1–5]. Constructed from either biological or non-biological materials, various de novo cell-like systems have been developed to simulate biological functions, ranging from exploring the origins of life to enabling cell-free biosynthesis[6–8]. The function of interacting with natural cells is an essential prerequisite for achieving sophisticated interplays between protocells and living systems, thereby enabling the development of advanced biological functions, such as in situ diagnostics and therapeutics[9–11]. However, current examples of artificial cells capable of interacting with live cells are scarce, primarily operating through diffusion-dependent pathways with natural signaling molecules or interactions with prokaryotic cells[12–15]. Hence, the development of artificial cells that can selectively communicate with mammalian cells and further precisely regulate their biological functions remains a significant challenge in this field.

Cell-cell communication is essential for biological processes in multicellular organisms, including homeostasis, regeneration, and immunity[16,17]. This communication can be categorized into two main models: the diffusion-dependent pathway (e.g. paracrine/endocrine) or the contact-dependent pathway[18,19]. In the diffusion-dependent model such as paracrine, signaling molecules are secreted by sender cells and diffuse to nearby areas, broadly affecting receiver cells. Conversely, the contact-dependent pathway offers more targeted and precise regulation. This pathway includes that a “sender” cell is activated by a specific stimulus and then presents ligands that selectively interact with a receiver cell through ligand–receptor interactions, ensuring direct and specific communication. Examples of contact-dependent communication include tissue-resident stem cells that facilitate wound healing[20], platelets that are integral to inflammation[21], and antigen-presenting cells (APCs) that are crucial for the adaptive

[1]State Key Laboratory of Chemo and Biosensing, Hunan University, Changsha, PR China. [2]College of Biology, Hunan University, Changsha, PR China. [3]College of Chemistry and Chemical Engineering, Hunan University, Changsha, PR China. [4]Key Laboratory of Quantitative Synthetic Biology, Shenzhen Institute of Synthetic Biology, Shenzhen Institutes of Advanced Technology, Chinese Academy of Sciences, Shenzhen, China. [5]Hunan Provincial Key Laboratory of Biomacromolecular Chemical Biology, Hunan University, Changsha, PR China. ✉e-mail: wanghonghui@hnu.edu.cn; niezhou.hnu@gmail.com

immune response[22]. While synthetic biology strategies like synNotch have advanced engineered cell-cell interactions within living systems, these approaches predominantly rely on top-down engineering of natural cells, leveraging their native machinery and protein-based elements[23–25]. In contrast, bottom-up artificial cell engineering introduces an orthogonal framework by constructing fully synthetic systems de novo, decoupled from the constraints of natural cells[26]. Inspired by the natural contact-dependent cell-cell communication mechanisms, the development of a designer artificial system capable of contact-dependent communication presents the potential to be an unprecedented way to precisely regulate mammalian cells. The key to this is a smart sender artificial cell that can respond to specific stimuli and alter its phenotypes to regulate living receiver cells. Nevertheless, the advancement of such systems is currently hindered, largely due to the lack of programmable and customizable molecular toolkits.

Recent advances in structural and dynamic DNA nanotechnology have held remarkable potential for bottom-up engineering of molecular systems with customizable structures and dynamic properties[27–30]. From a structural perspective, DNA molecules can self-assemble into intricate architectures across nanoscale to microscale dimensions in a programmable manner[31–35]. Additionally, the integration of functional nucleic acids (FNA), such as aptamers and DNAzymes, into molecular architectures enables the construction of stimuli-responsive systems with dynamic functions[36–42]. Utilizing DNA self-assembly approaches, artificial cells, also known as DNA protocells, have been developed to perform life-like functions or achieve inter-protocell interactions, primarily within artificial biomimetic systems[43–47]. However, the potential of constructing DNA-based artificial cells capable of responsively regulating mammalian cells via contact-dependent communication pathways has yet to be explored.

In this study, we have developed a bio-inspired design strategy for a DNA-empowered stimulable artificial cell designated to regulate mammalian cells, termed STARM (Fig. 1). Similar to a natural sender cell capable of contact-dependent communication, a STARM can be stimulated by specific stimuli (i.e., ion or light), transitioning from a resting state to an activated state to form contact-dependent communications between artificial cells and natural cells. This activation results in a desirable functional output, dynamically presenting artificial ligands to selectively interact with cognate receptors on a mammalian cell to achieve desired cellular functions. By utilizing a synergistic thermodynamically controlled strategy that incorporates heat-induced nucleobase-specific liquid–liquid phase separation (LLPS) followed by cooling-driven hybridization, STARMs spontaneously self-assemble from DNA-encoded copolymers to form a hierarchical cell-like structure with compartmentalization into artificial cell surface and cytoplasm-mimicking sub-compartments, respectively. Significantly, this assembly process of STARM is highly modular, allowing for the hierarchical integration of custom FNA-based modules, for instance aptamers and DNAzymes, with sensing and receptor regulation functionalities. The incorporation of auxiliary components, such as light-responsive gold nanorods (AuNRs), further reconfigures STARMs' functionality to respond to light stimuli. This modularity enables the facile rewiring user-defined stimuli to different outputs of mammalian cell regulation, including ion-induced chimeric prototissue formation and light-induced signal transduction mediated by receptor tyrosine kinase (RTK). Moreover, distinct designer STARMs

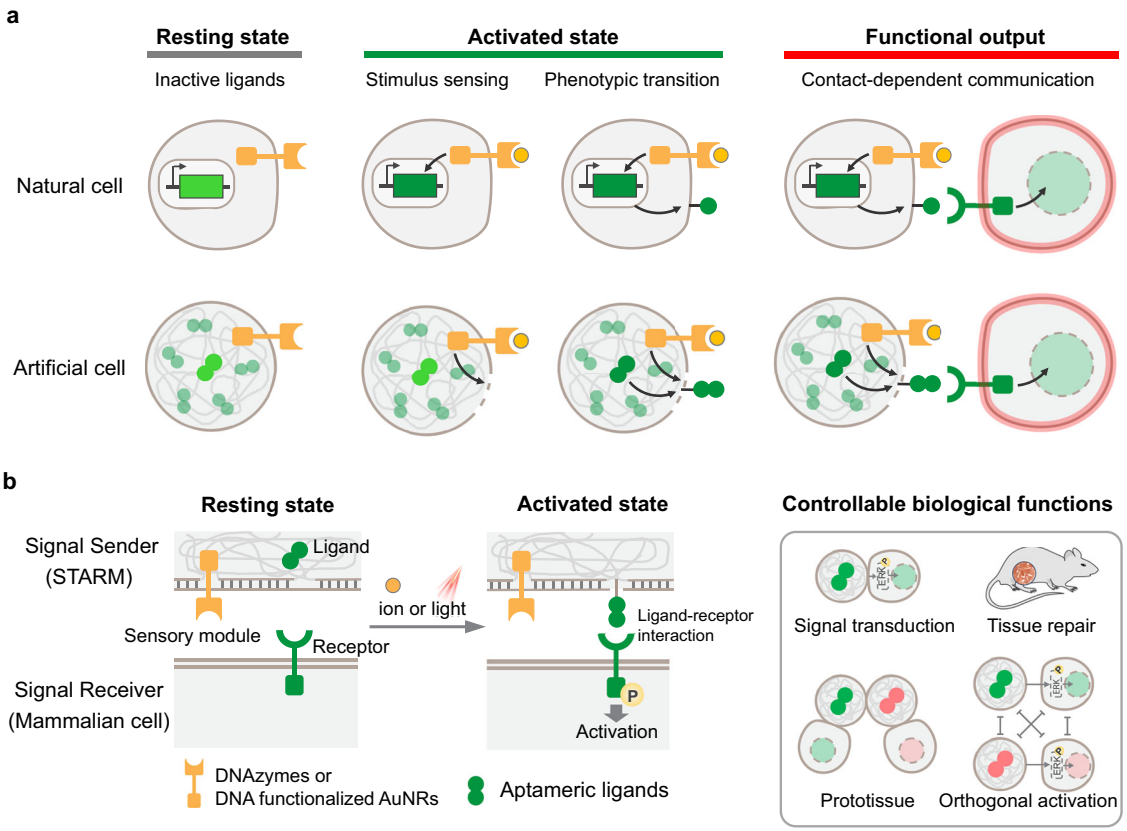

Fig. 1 | Schematic representation of STARM functionality. a Illustration of the simulation of natural, contact-dependent cell communication depicts the stages at which artificial cells transition from a resting to an activated state upon sensing specific stimuli. This transition enables the presentation of ligands that facilitate direct, contact-dependent communication with mammalian cells, leading to targeted cellular responses. **b** Depiction of the broader functionality of these stimulable artificial cells illustrates how they dynamically respond to stimuli such as ions or light. This response triggers a phenotypic transition, enabling various controlled biological functions, including signal transduction, the formation of chimeric prototissues, orthogonal signaling regulation and tissue regeneration in vivo.

equipped with unique input-output programs can be configured into a dual-channel circuit to orthogonally regulate different receptor-mediated signaling pathways in various mammalian cell types within a multicellular environment, demonstrating the scalability of the system. Furthermore, the light-responsive STARM has shown promise in facilitating deep tissue-penetrating near-infrared (NIR) light-induced tissue regeneration in living animals, underscoring its therapeutic potential in vivo. Thus, the strategy to engineer stimulable all-DNA artificial cells would open an avenue for developing intelligent artificial cell-based therapies.

Results

Design principle of a functional STARM

Our conceptual design of STARM is inspired by the contact-dependent communication pathway found in multicellular organisms (Fig. 1). This process involves a sender cell that responds to external stimuli by static-to-active transition and presents ligands to engage a receiver cell, ultimately regulating its receptor-mediated cellular signaling and behavior. Emulating these natural contact-dependent communications, STARM is rationally engineered to autonomously orchestrate a cascade of dynamic events. These events include sensing stimuli, transitioning phenotypes, and displaying surface-bound synthetic ligands that result in the functional outputs of desirable mammalian cell regulations through ligand–receptor interactions.

To enable sense-and-respond functionality, a STARM features an addressable surface-plasm structure that facilitates the spatial organization of the stimulus-sensing module and the receptor-interacting ligand modules respectively during its bottom-up construction. The outer surface of STARM is equipped with DNA-based sensory modules capable of responding to specific stimuli, closely mirroring the sensing capabilities of natural cell membranes. The inner plasm encapsulates aptameric ligands ready for modulating target mammalian cells via specific cell-surface receptors. Upon receiving an external stimulus, STARM undergoes a phenotypic transition that increases the permeability of its cell surface, allowing the aptameric ligands to be prominently displayed on the surface, which mimics the regulated secretory process of surface ligands of natural “sender” cells. This activation state empowers the STARM to engage in selective interaction with receptors on “receiver” mammalian cells or trigger receptor-mediated signal transductions. The programmability of the STARM strategy allows for customization of a broad range of cellular functions by easily tailoring the desired synthetic ligand-natural receptor pairs, representing an innovative synthetic platform for the precise regulation of mammalian cell behaviors.

Development of the all-DNA architecture for a STARM

To construct the surface-plasm architecture of STARM, we employed an all-DNA self-assembly system consisting of two types of single-strand DNAs (ssDNAs), Surface-DNA (artificial cell surface) and Plasm-DNA (artificial cytoplasm), each featuring repetitive multidomain structures (Fig. 2a and Supplementary Fig. 1). These ssDNAs, acting as building blocks for STARM, are designed to undergo heat-driven LLPS and cooling-induced duplex hybridization. Specifically, the repetitive multidomain of the Plasm-DNA includes a polyadenine (poly-A) domain for heat-induced LLPS behavior and A-T hybridization, an aptameric ligand domain for cellular interaction, and a plasm-location tag domain (p-tag) (Supplementary Table 1). The Surface-DNA features repetitive multidomain with a polythymidine (poly-T) domain for A-T hybridization at the outer layer, a substrate domain to accommodate the sensory module, and a surface-location tag domain (s-tag) (Supplementary Table 1). Both the Surface-DNA and Plasm-DNA were prepared via rolling circle amplification (RCA) synthesis, allowing for precisely tailored sequences within the multidomain constructs (Supplementary Fig. 2, Supplementary Methods).

The automated compartmentalization of Surface-DNA and Plasm-DNA localization is governed by their sequence-specific properties and thermodynamic behaviors. The heat-induced behaviors of Surface-DNA and Plasm-DNA were characterized by ultraviolet-visible (UV-vis) spectroscopy. In the presence of magnesium ions (Mg^{2+}, 50 mM), purine-rich Plasm-DNA exhibits LLPS behaviors at elevated temperatures, as evidenced by scattering in UV-vis spectra (Supplementary Fig. 3). Conversely, pyrimidine-rich Surface-DNA does not undergo phase separation across varying temperatures. Specifically, the phase diagram indicates that the cloud point temperature (T_{cp}) of Plasm-DNA, marking the onset of observable phase separation, is influenced by varying concentrations of Mg^{2+}. The T_{cp} starts at a cloud point temperature (T_{cp}) of approximately 75 °C at 10 mM Mg^{2+}, decreasing to around 45 °C at 100 mM Mg^{2+} (Fig. 2b). This purine-specific LLPS, driven by thermodynamics and Mg^{2+} ions, occurs as Mg^{2+} binds to purine residues, neutralizing negative DNA backbone charges and reducing electrostatic repulsion[33,46]. This charge neutralization promotes π−π stacking interactions and hydrogen bond formation, enabling the tight packing of purine-rich regions, leading to Plasm-DNA condensation into spherical coacervates. Conversely, Surface-DNA, enriched in pyrimidine bases, remains soluble under these conditions and does not undergo phase separation[33,44–46]. Importantly, the Plasm-DNA forms coacervates upon heating in the presence of 50 mM Mg^{2+} with a T_{cp} of 47 °C, which is approximately 13 °C lower than the melting point (T_m) of about 60 °C for poly-A/poly-T hybridization at the interface between Plasm-DNA and Surface-DNA (Supplementary Fig. 1). This temperature differential ensures that phase separation of Plasm-DNA precedes hybridization, allowing for the hierarchical assembly of the artificial cell architecture, with Plasm-DNA forming the core and Surface-DNA creating a stabilized shell at the periphery.

Subsequently, we assembled the artificial cells using Plasm-DNA and Surface-DNA, and their spatial arrangement was visualized using fluorescent probes: Alexa 488-p1*, complementary to the p-tag region in Plasm-DNA, and s*-TAMRA, complementary to the s-tag region in Surface-DNA (Fig. 2c and Supplementary Table 2). The assembly involved heating a mixture of ssDNAs from 25 °C to 95 °C, then cooling it stepwise back to 25 °C, which stabilized the phase-separated Plasm-DNA through hybridization (Supplementary Fig. 4). Using confocal laser scanning microscopy (CLSM), we observed that higher Plasm-DNA concentrations formed larger particles, reaching diameters up to 5.8 μm (Fig. 2c). The forward scattered light (FSC-A) of STARM were observed to rise with Plasm-DNA, indicative of the increase in particles size (Supplementary Fig. 5). Different molar ratios of Plasm-DNA to Surface-DNA influenced the microstructural arrangement within the all-DNA artificial cells. At a 1:0.25 molar ratio (Plasm-DNA: Surface-DNA), the assembly resulted in a uniform artificial cytoplasm enclosed by a thick cell surface (Fig. 2d). At a 1:0.5 ratio, we observed that Surface-DNA partially invaded the plasm compartment, whereas a 1:1 ratio formed a single nucleus-like structure within the architecture. Also, the side scattered light (SSC-A) of STARM were observed to rise at 1:0.5 and 1:1 molar ratio, indicative of the increase in their internal complexity (Supplementary Fig. 6). Therefore, optimal encapsulation for plasm-surface structure was achieved with concentrations of 10 μM for Plasm-DNA and 2.5 μM for Surface-DNA, with the molar ratio of 1:0.25. Further distribution analysis revealed that Plasm-DNA localized internally, akin to cytosol, while Surface-DNA lined the periphery, emulating a cell membrane (Fig. 2e). Notably, time-lapse fluorescence recovery after photobleaching (FRAP) analysis demonstrated a dynamic, liquid-like nature of the cytosol-like compartment, with a quick fluorescence recovery within 120 s (Fig. 2f and Supplementary Fig. 7). Interestingly, STARMs exhibit size-selective permeability, allowing efficient diffusion of small proteins (~3–5 nm) while restricting the entry of larger proteins (>5 nm), demonstrating their structured and selectively porous architecture (Supplementary Fig. 8 and Supplementary Table 3). These results establish optimal conditions for

https://doi.org/10.1038/s41467-025-57770-1

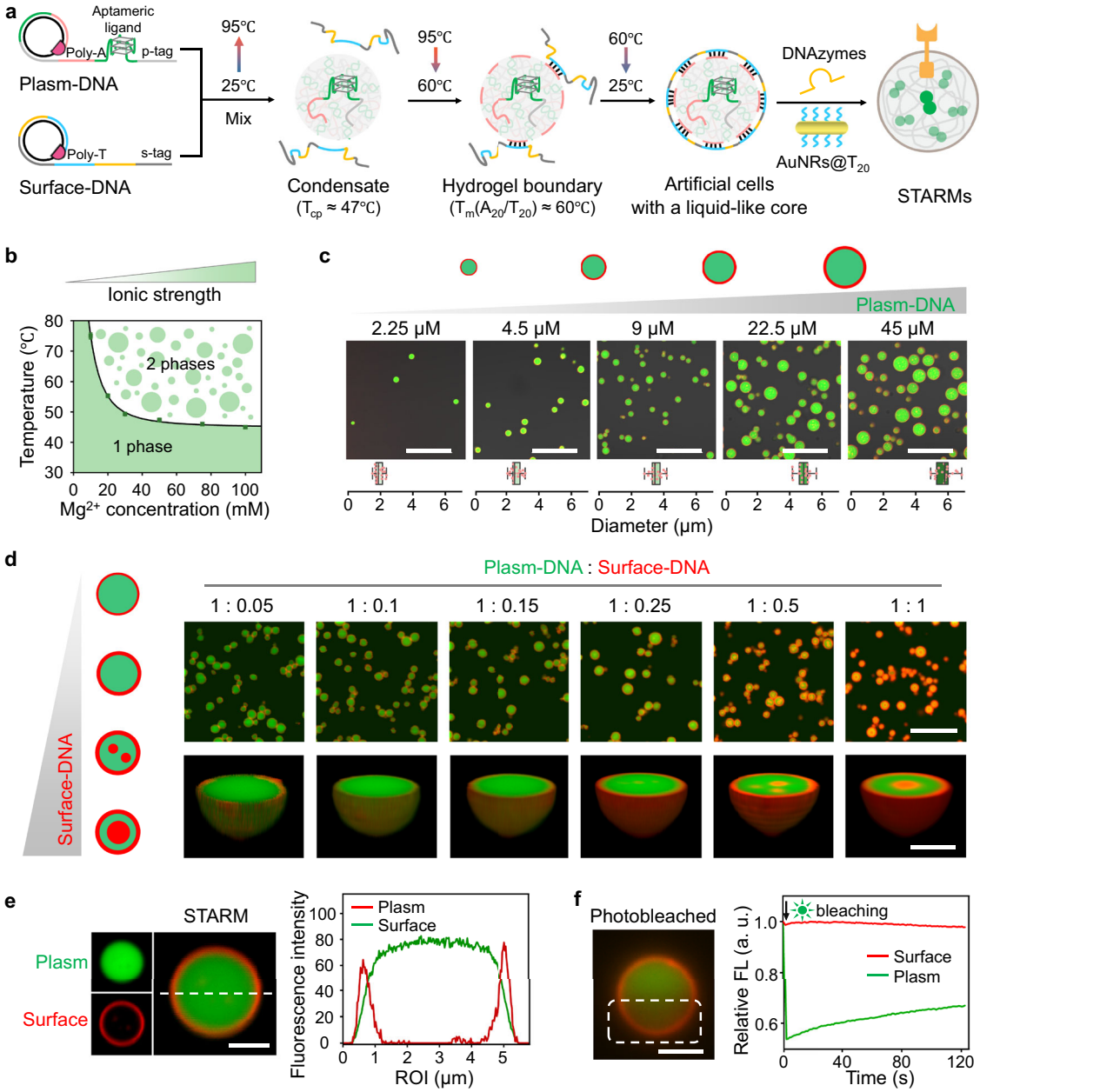

Fig. 2 | Development and characterization of architecture of STARMs. **a** Schematic representation of artificial cell assembly shows the formation of a plasm-surface structure with ssDNA multidomain copolymers. **b** Phase diagram displays the phase transition of Plasm-DNA under varying Mg^{2+} concentrations; temperature-phase diagrams illustrate transitions with increasing $MgAc_2$ concentration. Data represent mean ± standard deviation (s.d.) ($n = 3$ independent experiments). **c** Confocal laser scanning microscope (CLSM) images of DNA microarchitecture at various DNA concentrations, alongside a graph depicting particle size versus ssDNA concentration ($n = 20$ independent measurements). The center bar indicates median, bounds of box represent lower and upper quartiles, and the whiskers indicate minimum and maximum of the dataset for each group. Scale bar: 20 μm. **d** Morphological variations in artificial cells shown by adjusting the plasm to surface-DNA concentration ratios, with Plasm-DNA labeled by Alexa 488-p1* (green) and Surface-DNA by s*-TAMRA (red). Upper scale bar: 20 μm, lower scale bar: 2 μm. **e** A representative CLSM image of a STARM shows distinct compartmentalization with the plasm (green) and the surface (red). The dashed line indicates the cross-section analyzed in the right panel. Scale bar: 2 μm (Left panel). The fluorescence intensity profile across the STARM, illustrates the distribution of the Plasm-DNA (green) and Surface-DNA (red) compartments. The profile is measured along the dashed line shown in the left panel, spanning a total width of 5 μm (right panel). **f** Time-lapse fluorescence recovery after photobleaching (FRAP) images capturing dynamic recovery in the bleached area of an artificial cell highlights the mobility of Plasm-DNA (a.u. represents arbitrary unit). Scale bar: 2 μm. The experiments for (**c**–**e**) were repeated three times independently with similar results. Source data are provided as a Source Data file.

constructing the plasm-surface architecture of STARM, effectively mimicking the basic cell structure in nature.

Engineering an ion-responsive STARM

After establishing the architecture of the artificial cells, we proceeded to create functional STARMs capable of engaging in stimulus-induced, contact-dependent communication with mammalian cells through the responsive presentation of surface-bound synthetic ligands (Fig. 3a). As a first proof of concept, we developed an ion-responsive STARM with dynamic capabilities, encompassing metal ion sensing, aptameric ligand presentation for response, and subsequent interaction with receiver cells through ligand–receptor binding. Zinc ion (Zn^{2+}), a

https://doi.org/10.1038/s41467-025-57770-1

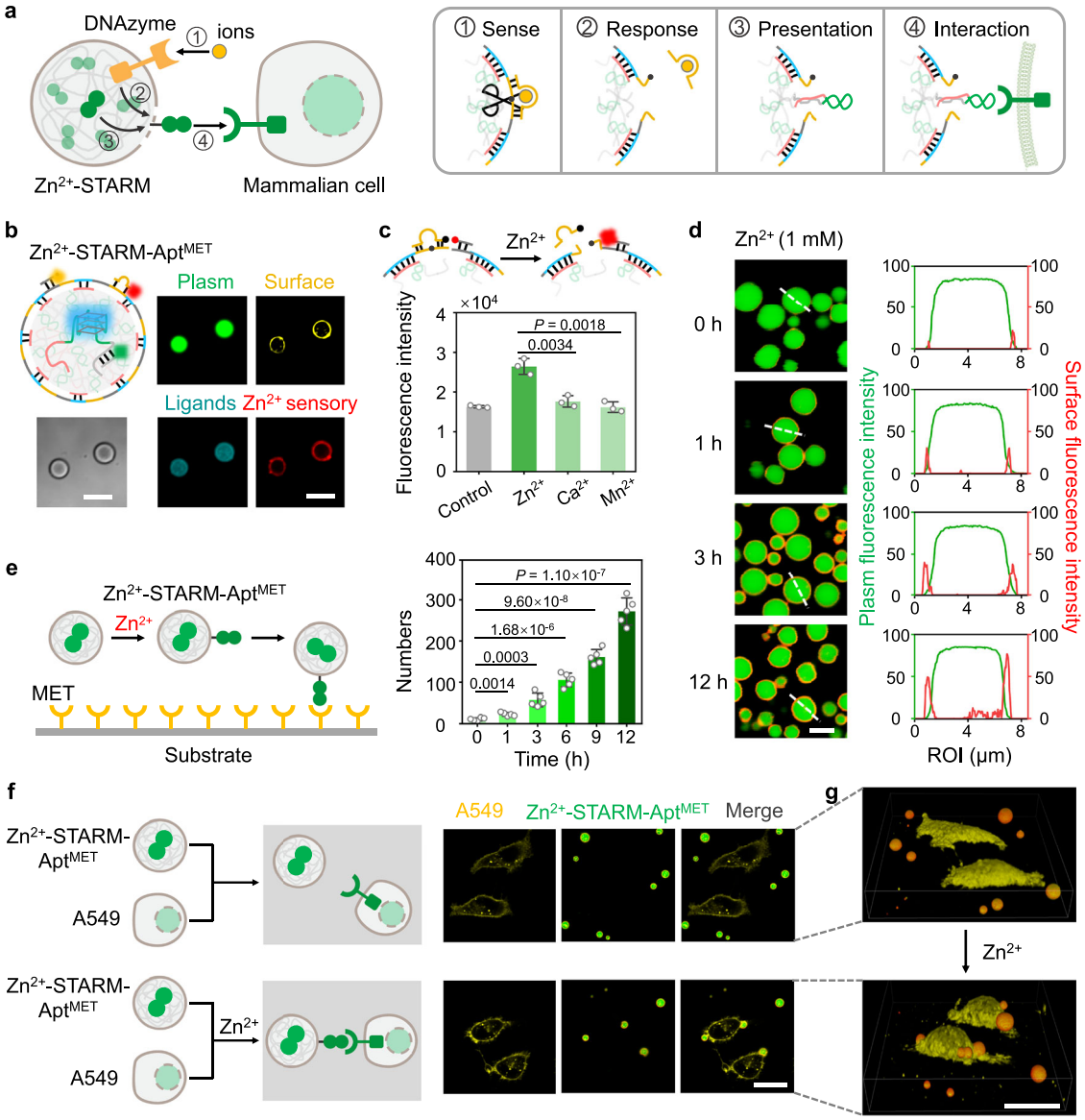

Fig. 3 | Construction and function of ion-responsive STARM. a Schematic representation of the Zn^{2+}-responsive STARM functioning. This includes ion sensing, response via aptameric ligand presentation, and subsequent engagement of receiver cells through ligand–receptor interactions. **b** CLSM images display the architecture of Zn^{2+}-STARM-Apt^{MET}, highlighting the Apt^{MET} ligand (cyan), the liquid-like plasm (green), and the Zn^{2+} responsive DNAzyme (red) at the surface (yellow). Scale bar: 5 μm. **c** Ion selectivity of Zn^{2+}-STARM-Apt^{MET} with Zn^{2+} (1 mM), Ca^{2+} (1 mM) and Mn^{2+} (1 mM) for 3 h. Data are shown as mean ± s.d. ($n = 3$ independent experiments). **d** Time-lapse CLSM images demonstrate the Zn^{2+} responsiveness of Zn^{2+}-STARM-Apt^{MET} by increasing TAMRA fluorescence at the surface upon exposure to Zn^{2+}. Scale bar: 5 μm. Linescan analysis accompanies to show fluorescence intensity of the plasm or surface in Zn^{2+}-STARM-Apt^{MET} after Zn^{2+} treatment. **e** Adhesion quantitative analysis displays the adhesion of Zn^{2+}-STARM-Apt^{MET} to recombinant MET protein-coated substrates post Zn^{2+} treatment. The histogram shows the quantification of the number of adherent Zn^{2+}-STARM-Apt^{MET} over time. Data represent mean ± s.d. ($n = 5$ independent experiments). **f** CLSM images demonstrate that Zn^{2+}-STARM-Apt^{MET} can exhibit contact-dependent communication with A549 cells in the presence of Zn^{2+} ions. A549 cells are stained with DiD (yellow), showing changes before and after Zn^{2+} treatment. Scale bars: 20 μm. **g** 3D reconstruction of the interaction between Zn^{2+}-STARM-Apt^{Sgc8} and A549 cells before and after $ZnCl_2$ (1 mM) treatment. Scale bar: 20 μm. The experiments for (**d**) and (**f**) were repeated three times independently with similar results. Two-tailed unpaired *t*-test was used for statistical analysis of (**c**, **e**). Source data are provided as a Source Data file.

biologically significant metal ion essential for tissue homeostasis[48], was employed as the example stimulus. The functional readout involved the utilization of an aptamer targeting the MET receptor (Apt^{MET}) chosen as the synthetic ligand to target MET-positive A549 cells. MET is a critical RTK predominantly found in epithelial cells and plays essential roles in regulating cellular signaling and behaviors[49]. In our design, a Zn^{2+}-sensitive DNAzyme was incorporated into the Surface-DNA as a sensory module, and a MET-binding aptamer was embedded as the plasm-encoded ligand for communication with recipient cells with highly expressed MET. Thus, this prototype of ion-responsive STARM can sense Zn^{2+} and respond by engaging MET-positive cells, denoted as Zn^{2+}-STARM-Apt^{MET}.

To assemble Zn^{2+}-STARM-Apt^{MET}, two DNA polymers were designed and synthesized, including a Surface-DNA containing the substrate domain for a Zn^{2+} DNAzyme, termed Zn^{2+}-Surface-DNA, and a Plasm-DNA encoding the ligand domain with the previously identified aptamer sequence for MET (40-mer, CLN0003)[50], named Plasm-DNA-Apt^{MET} (Supplementary Table 1 and Supplementary Fig. 9). Within the Zn^{2+}-STARM-Apt^{MET} architecture, the MET aptameric ligand, was visualized by its G-quadruplex (G4) structure via the G4-specific fluorogenic

probe NMNaI, a small molecule synthesized and characterized in our previous work[51]. NMNaI exhibits unique fluorescence properties upon binding to G4 structures, making it an effective probe for visualizing G4-containing aptamer, i.e., Apt^{MET}. Strong co-localization with Plasm-DNA labeled with Alexa 488-p* was observed (Fig. 3b and Supplementary Fig. 10). Meanwhile, the Zn^{2+} DNAzyme was labeled with Cy5, showing unexceptionable co-localization with s*-TAMRA-tagged Surface-DNA (Fig. 3b). These observations confirm the successful construction of Zn^{2+}-STARM-Apt^{MET} with the intended spatial arrangement of both the ion-sensing module and the functional output aptameric ligands.

We proceeded to assess the ion responsiveness of Zn^{2+}-STARM-Apt^{MET} by introducing a fluorophore-quencher reporter system, comprising a BHQ2-conjugated DNAzyme (BHQ2-DNAzyme) and a s*-TAMRA probe, which binds to the neighboring domains (the DNAzyme substrate domain and the s-tag domain) encoded within the Surface-DNA (Fig. 3c and Supplementary Table 2). This configuration ensures that the TAMRA fluorescence is quenched by the BHQ2 group in the resting state of STARMs. Activated by Zn^{2+} triggers the DNAzyme to cleave the substrate domain, causing the BHQ2-DNAzyme to detach from the Surface-DNA and the nearby s*-TAMRA fluorophore, which indicates ion sensing and substrate cleavage by the activated DNAzyme. Indeed, treatment with Zn^{2+} ions resulted in a time-dependent increase in TAMRA fluorescence compared to the control without Zn^{2+} treatment (Supplementary Fig. 11). The activation signal was primarily localized to the outer layer of the STARM (Fig. 3d). Quantitative analysis revealed approximately a 1.6-fold increase in TAMRA fluorescence signal upon activation with Zn^{2+} compared to controls treated with other divalent cations, such as Ca^{2+} and Mn^{2+}, underscoring the ion selectivity and specificity of the Zn^{2+}-STARM-Apt^{MET} (Fig. 3c).

Following the Zn^{2+} activation, we evaluated the functional outputs, specifically the increase in surface permeability of STARM to enable ligand presentation. Using a multi-well plate with functionalized bottom surfaces coated with recombinant MET protein, we investigated the ion-responsive ligand presentation of Zn^{2+}-STARM-Apt^{MET}. In the presence of Zn^{2+} ions, the STARMs gradually activated and exhibited preferential adhesion to the MET-functionalized substrate (Fig. 3e and Supplementary Fig. 12). Quantitative analysis demonstrated a significant enhancement in adhesion following 12 h of activation, with a 26-fold increase in the number of adherent STARMs compared to non-activated controls (Fig. 3e). The responsiveness of Zn^{2+}-STARM-Apt^{MET} is governed by the concentration-dependent kinetics of DNAzyme cleavage, highlighting the potential for further optimization of DNAzyme activity to improve reaction speed and efficiency. This selective enhancement in STARM adhesion to Zn^{2+} is attributed to the responsive presentation of an increased number of the aptameric ligands (Apt^{MET}), facilitating stronger interactions between the activated STARMs and the MET-enriched artificial interface.

Next, we explored the functionality of ion-activated STARMs in engaging with mammalian cells using a co-culture system with MET-positive A549 cells. Using the CSLM, we observed that in the resting state, Zn^{2+}-STARM-Apt^{MET} did not bind to A549 cells, indicating that Plasm-DNA-Apt^{MET} was well encapsulated. Upon Zn^{2+} stimulation, we observed that STARMs established direct contacts with live cells via selective interaction between Plasm-DNA-Apt^{MET} with MET receptor (Fig. 3f and Supplementary Figs. 13, 14). Quantitative analysis indicated that about 1.7 STARMs adhered to the surface of a single mammalian cell (Supplementary Fig. 15). In contrast, the variant STARMs that lacked the Zn^{2+}-DNAzyme module failed to exhibit the ion-responsive contacting behavior with A549 cells (Supplementary Fig. 14). Advanced three-dimensional (3D) reconstructions provided a more detailed view compared to 2D images, showing per single A549 cell that 2–3 spherical STARMs, with an average diameter of 4.4 μm, adhered in a direct contact manner (Fig. 3g and Supplementary Fig. 15). The contact-dependent communication mechanism of STARM is dependent on the presentation of responsive ligands and their subsequent binding to cellular receptors.

Moreover, STARMs demonstrated robust stability under different conditions. In the resting state, the STARMs could maintain structural integrity and functional activity for 24 h in 10% FBS, as shown by consistent thioflavin T (THT) fluorescence and morphology under light microscopy (Supplementary Fig. 16). Upon Zn^{2+} activation, STARMs retained their structural integrity and functional capability after 12 h of incubation with serum, confirming their robustness during extended activation (Supplementary Fig. 17). Additionally, STARMs stored at room temperature for 7 days exhibited high activation efficiency when stimulated with Zn^{2+}, highlighting their temporal stability and suitability for long-term applications (Supplementary Fig. 18). Together, our findings demonstrating the stability, responsiveness, and functionality of STARMs in interacting with MET-positive mammalian cells.

Ion-induced formation of chimeric prototissue

In nature, various cells have the ability to dynamically assemble into multicellular tissues through cell-cell adhesion processes during developmental and regenerative processes[52]. Inspired by this, we sought to explore the potential of STARM platform to artificially orchestrate the formation of chimeric prototissues, which are composed of both artificial cells and mammalian cell[45]. Our approach involved the design and synthesis of a series of ion-responsive STARMs, acting as sender cells, which were paired with different mammalian cell types known as receiver cells (Fig. 4a). By facilely integrating different aptameric ligand domains within the Plasm-DNA and assembling with Surface-DNA as well as Zn^{2+}-DNAzyme, we prepared two distinct types of Zn^{2+}-responsive STARMs with different functional outputs: Zn^{2+}-STARM-Apt^{Sgc8} and Zn^{2+}-STARM-Apt^{TD05} (Supplementary Table 1 and Supplementary Figs. 2, 19). To assemble the different STARMs, Plasm-DNA-Apt^{Sgc8} and Plasm-DNA-Apt^{TD05} were designed and synthesized. The former utilized Sgc8 aptamer, the known specific aptamer for protein tyrosine kinase 7 (PTK7) protein, as a ligand to target CEM cells with highly expressed PTK7, while the latter used TD05 aptamer as a cell-specific ligand to target Ramos cells[53] (Supplementary Fig. 20). Additionally, both Plasm-DNA constructs were encoded with complementary sequences (24 bp), allowing hybridization-based intercellular junctions between Zn^{2+}-STARM-Apt^{Sgc8} and Zn^{2+}-STARM-Apt^{TD05} to significantly increase the STARMs aggregation upon Zn^{2+} stimulation (Supplementary Fig. 21). We then employed a co-culture system to evaluate the ion-responsive interactions between mammalian cells and STARMs. The results showed that Zn^{2+}-STARM-Apt^{Sgc8} responsively bound to CEM cells in the presence of Zn^{2+}, whereas the variant STARM-Apt^{Sgc8} without Zn^{2+}-DNAzyme failed to response (Fig. 4b). Flow cytometry analysis revealed that Zn^{2+}-STARM-Apt^{Sgc8} bound specifically to CEM cells upon Zn^{2+} stimulation, with clustering increasing from 5.8% to 20.7% (Fig. 4c and Supplementary Fig. 22). Similarly, Zn^{2+}-STARM-Apt^{TD05} bound selectively to Ramos cells, with clustering rising from 2.2% to 19.1% under Zn^{2+} conditions (Supplementary Fig. 22). These results confirm the designed ion-responsive specificity of both STARMs.

To further explore the capacity of these STARMs in the development of chimeric prototissues, we conducted co-cultivation with two distinct mammalian cell types, CEM and Ramos, each paired with a specific variant of STARM (Fig. 4d). The CEM and Ramos cell lines were differentiated using various live-cell fluorescence dyes: the former was stained for the nucleus with Hoechst (blue), and the latter for the plasma membrane with DiI (yellow). The Zn^{2+}-STARM-Apt^{Sgc8} and Zn^{2+}-STARM-Apt^{TD05} variants were labeled with Alexa 488-p1* (green) and Cy5-p2* (red), respectively. Initially, in the absence of Zn^{2+}, the four differently fluorescently labeled cell types remained dispersed, with minimal assembly. However, upon Zn^{2+} stimulation, we observed the formation of chimeric assemblies consisting of both STARMs and the

https://doi.org/10.1038/s41467-025-57770-1

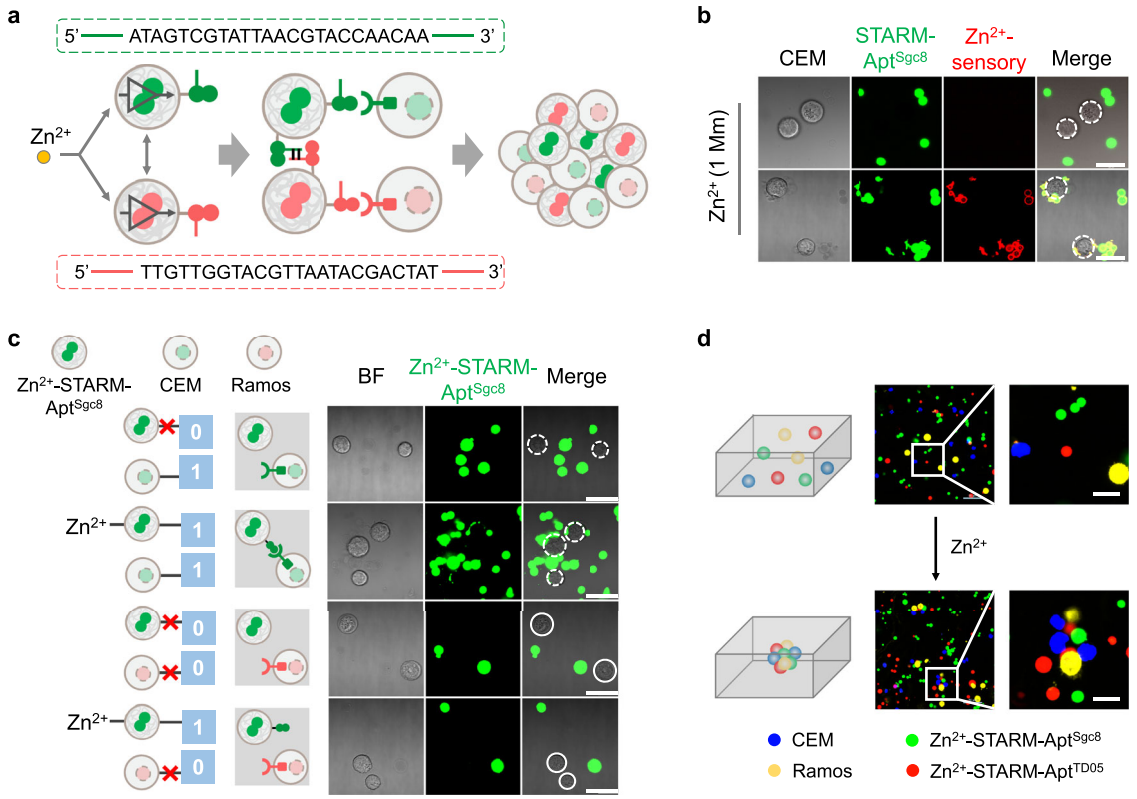

Fig. 4 | Ion-responsive chimeric prototissue formation. a Schematic illustration shows the formation of chimeric prototissues controlled by STARMs. The sequence depicts the STARMs interacting with and binding to natural cells upon stimulation with Zn^{2+}. **b** CLSM images display the interaction between Zn^{2+}-STARM-Apt^{Sgc8} or STARM-Apt^{Sgc8} and CEM cells after $ZnCl_2$ (1 mM) treatment. CEM cells are highlighted by white dotted circles. Scale bar: 20 μm. **c** CLSM images illustrate the co-culture of Zn^{2+}-STARM-Apt^{Sgc8} with CEM cells or Ramos cells, both in the presence and absence of $ZnCl_2$ (1 mM). CEM cells are indicated by white dotted circles, and Ramos cells by solid white circles. Zn^{2+}-STARM-Apt^{Sgc8} is labeled with Alexa 488. Scale bar: 20 μm. **d** CLSM images of showing a mixed population of cells including Zn^{2+}-STARM-Apt^{Sgc8}, Zn^{2+}-STARM-Apt^{TD05}, CEM, and Ramos cells, both with and without $ZnCl_2$ (1 mM). CEM cells are stained with Hoechst 33342 (blue), and Ramos cells with DiI (yellow). Zn^{2+}-STARM-Apt^{Sgc8} is labeled with an Alexa 488-p1* to tag the cytoplasm compartment (green), and Zn^{2+}-STARM-Apt^{TD05} with Cy5-p2* (red). Scale bars: 20 μm. The experiments for (**b**–**d**) were repeated three times independently with similar results.

CEM and Ramos cells (Fig. 4d). Detailed inspection revealed that these prototissues displayed a spatial organization where both STARMs were interconnected, associating with their respective target mammalian cells (Fig. 4d). Flow cytometry showed that Zn^{2+} stimulation led to a significant increase in the aggregation of the chimeric prototissue population, with the aggregation percentage rising from 2.6 ± 0.3% without Zn^{2+} to 14.2 ± 1.4% with Zn^{2+} activation, representing a 5.5-fold enhancement (Supplementary Fig. 23). The intercellular adhesion between CEM and Ramos cells were dependent on the presence of both Plasm-DNA-Apt^{Sgc8} and Plasm-DNA-Apt^{TD05}, respectively (Supplementary Fig. 24). Together, our findings demonstrate the potential of the STARM platform to tailor chimeric prototissue containing two distinct types of mammalian cells arranged as pre-designed, potentially offering a valuable tool for constructing synthetic tissues.

Light-responsive STARM for signaling regulation

Motivated by the modular characteristic, we conducted a study on the versatility of the STARM strategy by engineering a STARM designated to respond to light as a physical stimulus. In nature, light-responsive cells are capable of detecting light and initiating intercellular signaling, which is vital for biological processes such as phototropism[54,55]. To achieve light responsiveness, we integrated photothermally active AuNRs into the STARM design, which possessed the functional output to engage MET-positive cells for signaling regulation, denoted as Light-STARM-Apt^{MET} (Fig. 5a). To localize the light responsiveness to the surface of STARM, we prepared AuNRs coated with thiol-modified polythymine DNA (T_{20}-AuNRs, Supplementary Methods) and then co-assembled them with the complementary poly-A domain in Plasm-DNA-Apt^{MET}, as well as the Surface-DNA scaffold during STARM construction (Supplementary Fig. 25 and Supplementary Table 1). Using TAMRA-conjugated T_{20} (yellow), we visualized the distribution of T_{20}-AuNRs, which showed strong co-localization within the surface labeled by Cy5-s* (red) and not the plasm compartment tagged by Alexa 488 (green) (Fig. 5b and Supplementary Table 2).

Upon NIR light exposure, Light-STARM-Apt^{MET} demonstrated a time-dependent temperature increase, reaching approximately 38.5 °C within 10 min, whereas a negligible change observed in the STARM-Apt^{MET} variant lacking T_{20}-AuNRs (Supplementary Fig. 26). The photothermal effect induced by T_{20}-AuNRs led to the localized heat-induced melting of nearby A_{20}/T_{20} duplexes, enhancing surface permeability and enabling the display of Apt^{MET} for signaling regulation. Indeed, NIR light exposure significantly increased the binding of Light-STARM-Apt^{MET} to MET-functionalized surfaces, with more than a 31-fold increase in bound STARMs observed (Fig. 5c and Supplementary Fig. 27). CLSM observation of co-cultures revealed that light-activated STARMs significantly interacted with MET-positive A549 cells (Fig. 5d). Three-dimensional reconstructions (3D) showed a substantial number of uniformly sized spherical STARMs closely associating with each mammalian cell, in contrast to the minimal interactions observed in non-irradiated controls (Fig. 5e). Quantitative analysis indicated an average of 5.9 STARMs bound per cell (Supplementary Fig. 28).

Moreover, the aptameric ligands integrated within STARMs can be customized with dual output functionality, not only enabling cell interaction but also enhancing receptor targeting and signaling

https://doi.org/10.1038/s41467-025-57770-1

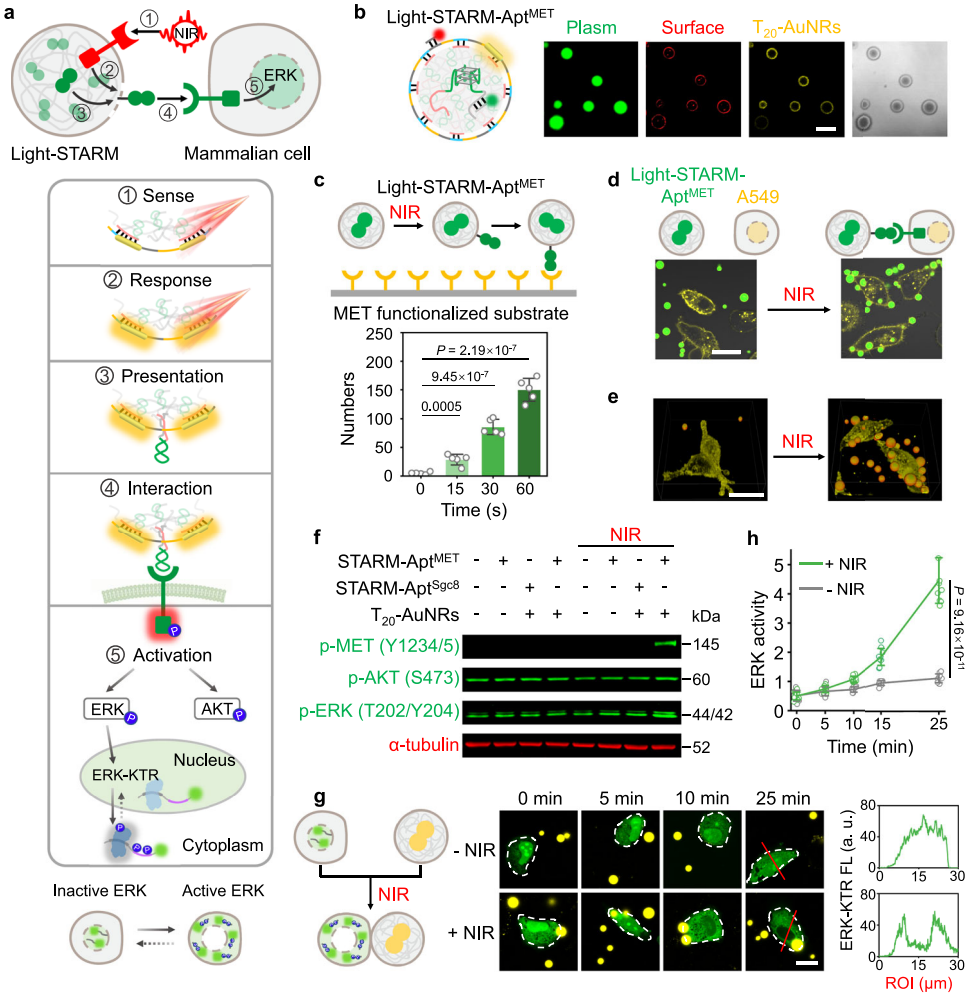

Fig. 5 | Light-responsive STARM for mammalian cellular signaling regulation. **a** Schematic illustration of Light-STARM-Apt^{MET} operation, including light detection, phenotypic alteration, and ligand presentation for contact-mediated communication and MET-AKT-ERK signaling axis regulation in mammalian cells. **b** CLSM images of Light-STARM-Apt^{MET} featuring gold nanorods (AuNRs) as light sensors. NIR light exposure induces photothermal effects that disrupt DNA structures, enabling ligand exposure. Scale bar: 5 μm. **c** The binding events of Light-STARM-Apt^{MET} to recombinant MET protein-functionalized substrates under NIR light. Data are presented as mean ± s.d. ($n = 5$ independent experiments). **d** CLSM images demonstrate the binding of Light-STARM-Apt^{MET} to A549 cells post-NIR light treatment. Scale bar: 20 μm. **e** Three-dimensional reconstructions validate contact-dependent communication between Light-STARM-Apt^{MET} and A549 cells upon NIR light exposure. Scale bar: 20 μm. **f** Western blot analysis of MET, AKT, and ERK phosphorylation levels in A549 cells after NIR light interaction with Light-STARM-Apt^{MET}, signifying the initiation of cellular signaling. **g** Fluorescence microscopy images of ERK-kinase translocation reporter (ERK-KTR) in A549 cells, visualizing ERK pathway activation in response to Light-STARM-Apt^{MET} under NIR light. Scale bar: 20 μm. Linescan analysis accompanies to show ERK-KTR translocation dynamics in A549 after Zn^{2+} treatment for 25 min. **h** Quantitative assessment of single-cell ERK activity, measured by the ratio of cytoplasmic to nuclear fluorescence intensity over time following Light-STARM-Apt^{MET} activation by NIR light (a.u. represents arbitrary unit). Data are presented as mean ± s.d. ($n = 10$ independent measurements). The experiments for (**d**) and (**f**) were repeated three times independently with similar results. Two-tailed unpaired *t*-test was used for statistical analysis of (**c**, **h**). Source data are provided as a Source Data file.

modulation. This integration facilitates the initiation of specific signal transduction pathways in mammalian cells. Specifically, within the design of Light-STARM-Apt^{MET}, the aptameric ligand, Plasm-DNA-Apt^{MET} not only selectively bound to MET-expressing A549 cells but also facilitated MET phosphorylation (Y1234/5) (Supplementary Fig. 13). This signaling activation effect is attributed to the multivalent interaction of Apt^{MET} of STARM that promotes MET oligomerization and subsequent autophosphorylation[35]. At the resting state of Light-STARM-Apt^{MET}, this signaling-regulating function of Plasm-DNA-Apt^{MET} was entirely enclosed within the architecture of STARM, without promoting MET signaling. However, upon exposure to light, the STARMs were activated, initiating MET signaling and downstream signaling pathways (AKT and ERK) within A549 cells (Fig. 5f and Supplementary Fig. 29). Interestingly, MET phosphorylation peaked at 5 min in A549 cells, followed by a rapid decline, consistent with intrinsic cellular feedback mechanisms such as receptor internalization and phosphatase-mediated dephosphorylation[56,57]. Following MET activation, Light-STARM-Apt^{MET} propagated downstream signaling cascades, inducing the phosphorylation of ERK1/2 (T202/Y204) in a time-dependent manner, with sustained activation observed from 5 to 60 min (Supplementary Fig. 29). This dynamic regulation of the MET-ERK-AKT signaling axis demonstrates the capability of the light-responsive STARM platform to achieve precise control and effective modulation of cellular signaling.

To further visualize the contact-dependent communication and signaling activation at the single-cell level, we introduced an ERK-kinase translocation reporter (ERK-KTR) fused with the Clover protein[58]. This system allowed real-time monitoring of ERK activity, shifting from nuclear to cytoplasmic upon phosphorylation, providing a dynamic and quantitative measure of ERK response (Fig. 5a). Upon NIR light exposure, a pronounced and sustained ERK response was observed in A549 cells in contact with Light-STARM-Apt^{MET} (Fig. 5g).

We quantified the cytoplasmic/nuclear ratio of ERK-KTR signal as an assessment of ERK activity. In the presence of Light-STARM-Apt^{MET}, the ERK activity within a single cell increased in a time-dependent manner, reaching a maximum 4.0-fold increase at 25 min, compared to non-stimulated condition (Fig. 5h). This observed dynamic in ERK response aligns with the phosphorylation patterns of ERK1/2 as indicated by bulk cell lysates western blot analysis (Supplementary Fig. 29). Collectively, these results illustrate the effective development of a light-responsive STARM that can facilitate contact-dependent communication and trigger activation of MET and its downstream ERK signaling upon exposure to NIR light.

Establishing a dual-channel circuit for orthogonal signaling control

Our success in customizing STARM to respond to user-defined stimuli has provided a fundamental framework for constructing different stimuli-responsive control systems for cell signaling and behavior. However, achieving precise control using artificial cells in complex multicellular systems remains challenging due to potential interference in ligand–receptor interactions and signaling regulation between different cell types. This challenge necessitates the development of a multichannel circuit capable of orthogonal control over distinct signaling pathways in a cell-specific manner[59,60]. We envision that the versatility of the STARM platform allows for the establishment of a dual-channel circuit integrating two distinct STARMs, each with unique input-output programs without crosstalk. This enables orthogonal control over receptor-mediated signaling in different mammalian cell types within multicellular environments (Fig. 6a).

In the proposed dual-channel circuit, we identified the first STARM component as Zn^{2+}-STARM-Apt^{MET}, functioning in Zn^{2+} responsive, contact-dependent communication with MET-positive cells for signaling regulation. For the second component, we developed Light-STARM-Apt^{FGFR1}, a light-responsive STARM to engage and activate fibroblast growth factor receptor 1 (FGFR1) signaling. FGFR1 is an important RTK predominantly expressed in fibroblasts and neural stem cells and is essential for regulating proliferation and differentiation[49]. For evaluating Light-STARM-Apt^{FGFR1}, we selected NIH3T3 cells, an FGFR1-positive murine fibroblast cell line.

The construction of Light-STARM-Apt^{FGFR1} involved synthesizing Plasm-DNA-Apt^{FGFR1} (encoding the 38-mer aptamer SL38 for FGFR1[61,62]) and co-assembling it with T_{20}-AuNRs and Surface-DNA-light (Supplementary Table 1 and Supplementary Fig. 30). Flow cytometry and western blot analysis showed that Plasm-DNA-Apt^{FGFR1} and Plasm-DNA-Apt^{MET} specifically bind to NIH3T3 cells and A549 cells, respectively, without cross-interference, activating AKT and ERK phosphorylation signaling pathways respectively in their target cells (Supplementary Fig. 31). Furthermore, in the resting state, neither STARM binds to its target cells (Supplementary Fig. 32). Light-STARM-Apt^{FGFR1} is activated only by NIR light, leading to selective binding to NIH3T3 cells and inducing light-responsive cellular signaling and proliferation (Supplementary Figs. 32–34). Conversely, Zn^{2+}-STARM-Apt^{MET} is specifically activated by Zn^{2+}, facilitating targeted binding to A549 cells and inducing MET-mediated AKT and ERK phosphorylation without impacting NIH3T3 cells (Supplementary Figs. 32–34). Consequently, the cell-specific targeting capabilities of Zn^{2+}-STARM-Apt^{MET} and Light-STARM-Apt^{FGFR1} towards A549 and NIH3T3 cells, respectively, render these two distinct STARMs highly suitable for an orthogonal dual-channel regulation system.

To examine the functionality of the dual-channel circuit, we set up a co-culture system with separate seeding regions for A549 and NIH3T3 cells using a multicell co-cultivation apparatus (Supplementary Fig. S35). To visualize and quantitatively analyze the contact communication between mammalian cells and STARMs, we labeled Light-STARM-Apt^{FGFR1} with Cy5-p2* and Zn^{2+}-STARM-Apt^{MET} with Alexa 488-p1*. These STARMs were then mixed and added to the co-cultivation system and activated by Zn^{2+} or NIR light. In the absence of stimulation, a baseline level of four types of STARM-mammalian cell contact events with similar quantities was observed (Fig. 6b and Supplementary Fig. 35). Following Zn^{2+} stimulation, the interaction events between STARM and mammalian cells significantly increased by 2.6-fold compared to the untreated group, mainly attributed to the interaction of Zn^{2+}-STARM-Apt^{MET} with A549 cells, while showing minimal crosstalk with NIH3T3 cells (Fig. 6b and Supplementary Fig. 35). Alternatively, NIR stimulation increased the overall STARM-mammalian cell interaction events by 2.9-fold compared to the untreated group, primarily due to the binding of Light-STARM-Apt^{FGFR1} with NIH3T3 cells, rather than A549 cells (Fig. 6b and Supplementary Fig. 35). These results indicate that the dual-channel circuit facilitates accurate regulation of interaction events between artificial cells and mammalian cells within a heterogeneous cell population under defined stimulation parameters.

We next investigated the effect of controlled contact-dependent communication on cell-specific signal activation. The spatial separation of A549 and NIH3T3 cells in the co-culture system allowed us to examine the cell-specific signal activation by the dual-channel circuit. The in situ immunofluorescence staining was used to image and quantify phosphorylated AKT and ERK levels, both of which are downstream signaling pathways of MET and FGFR. Consistent with the results on cell-specific communication, we confirmed that NIR light significantly induced AKT and ERK phosphorylation in the NIH3T3 cell region due to Light-STARM-Apt^{FGFR1} activation, while Zn^{2+} had no effect despite the presence of Zn^{2+}-STARM-Apt^{MET} (Fig. 6c and Supplementary Fig. 36). Conversely, Zn^{2+} promoted AKT and ERK signaling primarily in the A549 cell-seeded region, without affecting NIH3T3 cells under NIR light (Fig. 6c and Supplementary Fig. 36).

Furthermore, we conducted single-cell level studies to explore the correlation of ERK activity in ERK-KTR-transfected A549 and NIH3T3 cells with the contact-dependent communication using dual-channel circuit (Fig. 6d). The results showed that Zn^{2+} stimulation led to a pronounced ERK response in A549 cells, but not in NIH3T3 cells (Fig. 6e). Conversely, NIR light exposure promoted ERK response in NIH3T3 cells with minimal impact on A549 cells. Line segment analysis of single typical cell in different conditions revealed that Zn^{2+} stimulation led to decreased ERK fluorescence in the nucleus of the A549 cell that interacted with Zn^{2+}-STARM-Apt^{MET}, compared to unaffected cells without stimulation (Fig. 6e). Similarly, NIR light exposure selectively promoted a decrease of ERK fluorescence in the nucleus of an NIH3T3 cell adhering to several Light-STARM-Apt^{FGFR1}. Collectively, our findings confirm the effectiveness of the dual-channel STARM circuit in orthogonally controlling signaling pathways across different cell types within a complex multicellular context.

Therapeutic potential of designer STARM in vivo

We next investigated the potential of engineered STARMs for artificial cell-based therapy in vivo by using a skeletal muscle injury animal model (Fig. 7a). Upon injury, the skeletal muscle regeneration depends on FGFR signaling to activate the regenerative stem cells within muscle tissues for growth and differentiation[63]. Given that muscle injuries occur beneath the skin, an optimal therapeutic approach would require the ability to control cells at depth within the tissue. Light-STARM-Apt^{FGFR1}, with its potential for NIR light-guided cellular control, is particularly promising due to its responsiveness to deep tissue-penetrating NIR light at 808 nm[64,65]. To evaluate the in vivo behavior of Light-STARM-Apt^{FGFR1}, fluorescence imaging revealed that Light-STARMs remained localized at the injection site for up to 12 h before gradually clearing over 24–48 h, which were primarily detected in the kidneys and liver, indicating systemic distribution and clearance pathways. Serum analysis further confirmed a time-dependent reduction in circulating fluorescence, reflecting efficient clearance of Light-STARMs (Supplementary Fig. 37).

https://doi.org/10.1038/s41467-025-57770-1

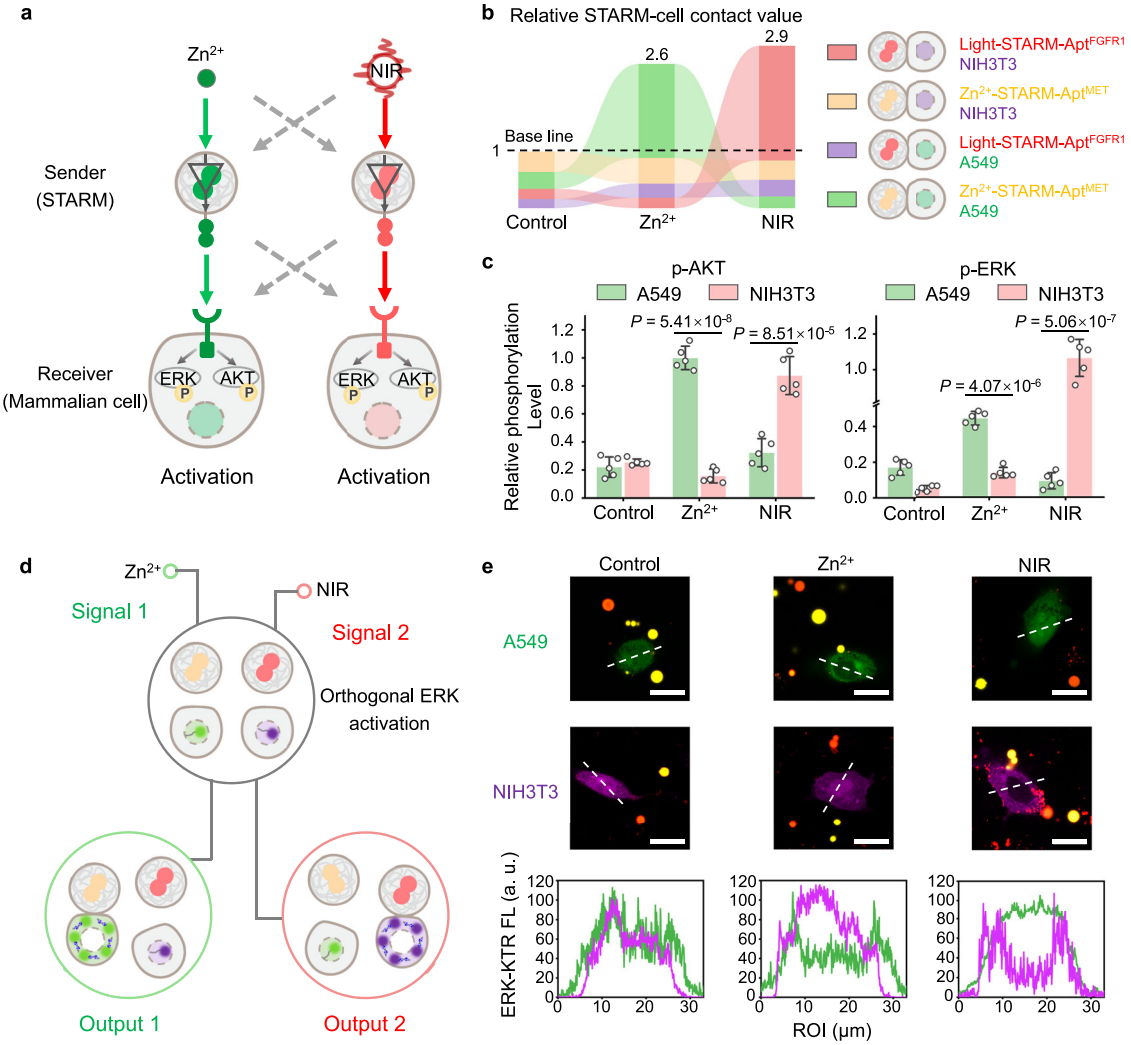

Fig. 6 | Dual-channel STARM circuit enables orthogonal regulation of signaling pathways in mammalian cells. a Schematic illustration of the dual-channel STARM circuit designed for orthogonal activation by Zn^{2+} and NIR light. The circuit combines ion-responsive and light-responsive STARMs for targeted cellular activation. **b** Quantification of STARM-cell contact events in co-cultured A549, NIH3T3, Zn^{2+}-STARM-Apt^{MET}, and Light-STARM-Apt^{FGFR1} cells under Zn^{2+} or NIR light treatment. For each experimental condition, the contact values were calculated based on 125 analyzed A549 or NIH3T3 cells, and the relative contact values were derived to demonstrate the effects of Zn^{2+} and NIR stimuli (Supplementary Fig. 35). **c** In situ immunofluorescence analysis demonstrating AKT and ERK phosphorylation in co-cultured A549 and NIH3T3 cells treated with the dual-channel STARM circuit under $ZnCl_2$ (1 mM) or NIR light (1 W/cm^2). Data represent mean ± s.d. ($n = 5$ independent experiments). **d** Schematic illustration of the dual-channel STARM circuit designed for ERK orthogonal activation by Zn^{2+} and NIR light in a multicell co-cultivation environment. **e** Visualization of ERK response in A549 and NIH3T3 cells using ERK-KTR Clover plasmids. Cells show differential ERK translocation under Zn^{2+} or NIR light conditions. The green and purple channels indicate ERK-KTR Clover in A549 and NIH3T3 cells, respectively, with TAMRA labeling Zn^{2+}-STARM-Apt^{MET} (yellow) and Cy5 for Light-STARM-Apt^{FGFR1} (red). Scale bars: 20 μm. Linescan analysis accompanies to show ERK-KTR translocation dynamics in both cell types. Two-tailed unpaired *t*-test was used for statistical analysis of (**c**). Source data are provided as a Source Data file.

To establish the muscle injury model, mice were administered cardiotoxin (CTX) to the tibialis anterior once daily for three consecutive days (Fig. 7b). This approach effectively disrupted myofibers and damaged the sarcomere structure within the injured muscle, as confirmed by histological analysis (Fig. 7c). Following the 3-day injury induction, Light-STARM-Apt^{FGFR1} was injected into the injured site, and the area was treated with 3 min of daily NIR light irradiation. This duration was carefully selected based on prior optimization experiments, demonstrating over 90% cell viability at this irradiation time, thereby ensuring effective stimulation while minimizing cytotoxicity (Supplementary Fig. 38).

To assess the immediate effects of the treatment, mice were euthanized 30 min post-NIR light irradiation, and immunofluorescence analysis was performed on muscle tissue sections. The results showed strong co-localization of p-FGFR1 signals (red) with Cy5-labeled Light-STARM-Apt^{FGFR1} (yellow), confirming that FGFR1 signaling activation was mediated by the aptameric ligands' presentation from activated STARMs. This precise spatial alignment highlights the ability of Light-STARM-Apt^{FGFR1} to achieve targeted activation of FGFR1 signaling in Pax7-positive muscle stem cells while minimizing off-target effects (Supplementary Fig. 39). The therapeutic regimen, consisting of 3 consecutive days of Light-STARM-Apt^{FGFR1} injection and NIR light treatment, was then evaluated for its regenerative effects. Histological analysis revealed an increase in muscle fiber area and nuclei count at the injury site, indicative of enhanced muscle regeneration (Fig. 7d). The activation of muscle stem cells was assessed through immunostaining with Pax7, a key transcription factor involved in myogenesis[66]. A notable increase in Pax7-positive cells within the injured area suggested a controlled recruitment of muscle stem cells. In contrast, Pax7-positive cells were absent in the injured regions of the control group, which included animals injected with STARM without NIR light treatment or those that received NIR light

https://doi.org/10.1038/s41467-025-57770-1

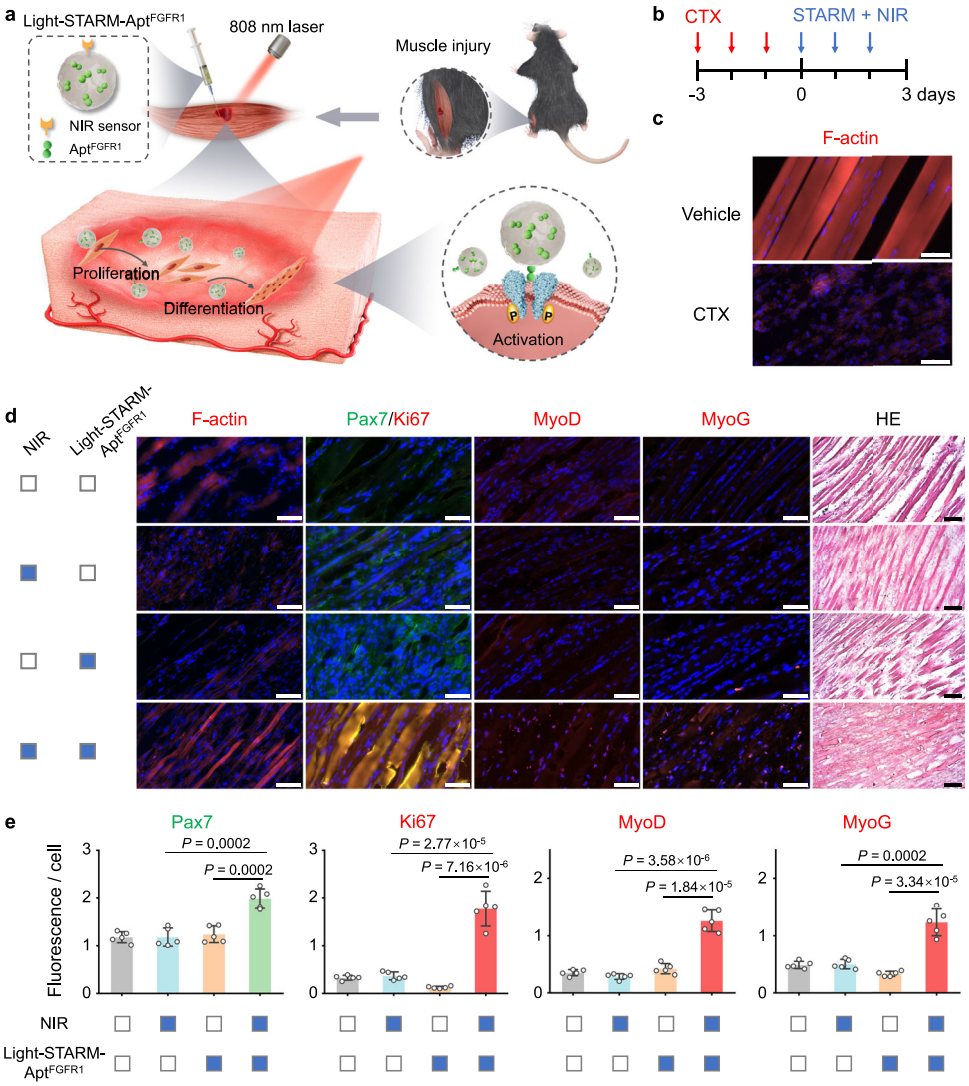

Fig. 7 | Designer STARMs promote light-driven tissue regeneration in vivo. **a** Schematic of the experimental setup for a skeletal muscle injury model in mice, targeting the tibialis anterior muscle. The procedure involves the use of an 808 nm laser for NIR light treatment following cardiotoxin (CTX) injections to induce muscle damage. **b** Experimental design and time line of TA muscle injury, STARM + NIR light treatment, and analysis in mice ($n = 4$ mice per group). **c** Representative images of skeletal muscle pre- and post-CTX administration, highlighting the induced muscle injury. Myofibers are stained for F-actin (red) and nuclei (DAPI, blue) to illustrate tissue architecture changes. Scale bar: 50 μm. **d** Immunofluorescence staining of muscle sections post-injury, treated with NIR light alone or in combination with Light-STARM-Apt^{FGFR1}. Staining includes F-actin, Pax7, Ki67, MyoD, and MyoG to assess muscle repair and regeneration. Hematoxylin and eosin (H&E) staining displays overall muscle tissue morphology. Scale bars: F-actin, Pax7, Ki67, MyoD, and MyoG–50 μm; H&E–500 μm. **e** Quantitative analysis of muscle satellite cell activation and the myogenic process, measuring fluorescence intensity for myogenic markers (Pax7, Ki67, MyoD, and MyoG) in high-power field (HPF) sections from treated mice. Data represent mean ± s.d. ($n = 5$ independent measurements). The experiments for (**c**) were repeated four times independently with similar results. Two-tailed unpaired *t*-test was used for statistical analysis of (**e**). Source data are provided as a Source Data file.

treatment without Light-STARM-Apt^{FGFR1} injection. This indicates that the mobilization of stem cells was due to the NIR light-activated STARMs (Fig. 7d).

Furthermore, these activated Pax7-positive cells are expected to proliferate and differentiate into mature skeletal muscle cells, thereby promoting cellular repair and regeneration. In order to track the expansion of muscle stem cells, we employed a Ki67 antibody, which identifies cells in the cell cycle phase preceding cell division. The biological relevance of Ki67 staining resides in its utility as a marker for discerning proliferating cells within a tissue specimen. We found a significant increase in Ki67$^+$/Pax7$^+$ cells, demonstrating that light-activated signaling enhances muscle satellite cell proliferation (Fig. 7d, e). Additionally, the Pax7-positive cell population showed a marked upregulation in the expression levels of MyoD and MyoG, which are early markers of muscle regeneration[67,68]. This upregulation indicated the initiation of myogenic differentiation for the generation of new muscle fibers (Fig. 7d, e). In addition to their therapeutic efficacy, Light-STARM-Apt^{FGFR1} demonstrated excellent biocompatibility, with no detectable adverse effects on the blood system, as evidenced by hematological analyses (Supplementary Fig. 40). Together, our study in vivo provides the example of responsive artificial cells facilitating light-guided skeletal muscle regeneration in living animals, potentially opening up avenues for the advancement of synthetic therapeutics.

Discussion

In this study, we have developed a DNA nanotechnology-based platform for the bottom-up construction of stimuli-responsive all-DNA-based artificial cells, namely STARMs, designed for the precise modulation of mammalian cell behaviors. These de novo designed

synthetic entities are poised to mimic the dynamic and life-like characteristics of natural cells, which is crucial for advancing the design and engineering of artificial cells to effectively communicate with and regulate live cells, and for the development of intelligent therapies. Drawing inspiration from contact-dependent communication mechanisms in biological systems, STARMs are equipped to sense and respond to specific stimuli, engaging in biomimetic ligand–receptor interactions for contact-dependent communication with mammalian cells, offering significant potential for controllable cell communication and precise cellular function regulation.

The design and functionality of STARMs represent a significant advancement in artificial cell technology, offering programmable and customizable molecular toolkits for controllable communication between artificial cells and natural cells. Unlike traditional synthetic biology strategies, such as synNotch[23,25] and SynCAM[69], which focus on top-down engineering of mammalian cells by modifying native cell-cell interaction receptors, STARMs represent a fully bottom-up approach enabling de novo reconfiguration of contact-dependent communication between artificial and natural cells via programmable ligand–receptor interactions[12–15]. This bottom-up artificial cell strategy offers unique advantages, enabling the design of artificial cells independent of genetic constraints or reliance on pre-existing natural cellular mechanisms[26]. Specifically, DNA-empowered STARMs can dynamically transition from a resting state to an activated state in response to user-defined stimuli, presenting synthetic ligands for programmable and responsive communication. By complementing existing top-down approaches, STARM strategy would expand the toolkit for orthogonal, modular regulatory to achieve sophisticated and customizable contact-dependent communication with mammalian cells.

Leveraging structural and dynamic DNA nanotechnology, our modular STARM strategy represents a significant advancement in functional artificial cell construction. The hierarchical assembly of functional modules allows STARMs to flexibly integrate custom input-sensing modules and output aptameric ligand modules within their all-DNA framework. In our work, we have demonstrated that the input-sensing modules can be customized for ion responsiveness or light responsiveness, while the output synthetic ligand modules are tailored to target and activate different cell types with their specific receptors, such as MET-positive epithelial cells and FGFR1-positive fibroblasts or stem cells. This versatile combination of input-output paradigms enables the reconfiguration of user-defined stimuli-responsiveness to achieve various targeted cell manipulations, including ion-regulated chimeric prototissue assembly and light-induced signal activation. Unlike "always-on" natural ligands, aptameric ligands or ligand-decorated DNA nanostructures, STARMs present ligands responsively for selective cell regulation in complex multicellular environments. The dual-channel circuit further demonstrates their capacity for orthogonal control of AKT and ERK signaling in distinct mammalian cell types. However, considering that the responsiveness and functionality of STARMs could be influenced by their size distribution, further optimization to improve size homogeneity would enhance reproducibility and ensure robust signaling activation. This refinement would bolster the ability of STARMs to consistently and effectively regulate mammalian cells in complex biological systems.

Significantly, while instances of artificial cells employed for in vivo therapy remain relatively rare, we have successfully designed and implemented STARMs specifically tailored for tissue regeneration scenarios. By leveraging the NIR light-responsive sense-and-respond functionality, Ligh-STARM-Apt^{FGFR1} exhibits selective recruitment and robust regulation of the tissue-resident stem cells through FGFR1-mediated mechanisms, thereby facilitating in situ muscle regeneration in living organisms. Furthermore, the demonstrated stability and biocompatibility of STARMs ensure their sustained functionality and safety under physiological conditions, making them suitable for therapeutic applications. This achievement highlights the potential of STARMs as promising alternatives to conventional regenerative therapies[66]. Therefore, our STARM strategy addresses the unmet needs of current artificial cell methods in on-demand tissue regeneration, implying a potential avenue of in vivo therapeutic applications of smart artificial cells.

Looking forward, future research directions will focus on overcoming existing challenges to enhance the robustness, stability, and specificity of these artificial cells in complex biological environments. Efforts are required to expand the range of stimuli they can respond to by integrating sensory modules and refining their programmable features. Developing engineering STARMs with responsive circuits through the integration of DNA-based logical gates has the potential to yield enhanced functional outputs customized to meet specific therapeutic requirements. These artificial cells can be designed to carry out sophisticated communication protocols, resulting in intricate, feedback-driven control of biological systems. Moreover, our primary establishment of a dual-channel orthogonal control system paves the way for rationally organizing different types of STARMs into the multi-layered cellular communication networks, such as close-loop feedback systems. This potential could enable programmable and customized biological functions within biological systems, offering unprecedented precision in the regulation of complex biological processes.

In summary, we present an all-DNA-based synthetic platform that facilitates biomimetic contact-dependent communication with mammalian cells. This modular platform offers the ability to reconstitute user-defined stimuli for tailored engagement of specific cell types in signaling regulation. These artificial cells, composed entirely of DNA, provide a multifunctional and dynamic platform for programmable communication and signal regulation in mammalian cells, providing an innovative toolkit for the future development of intelligent therapeutics in biomedicine.

Methods

Oligonucleotides

All oligonucleotide sequences presented in Supplementary Tables 1, 2 were synthesized by Sangon Biological Engineering Technology & Co., Ltd (Shanghai, PR China).

Synthesis of ssDNA polymers using rolling circle amplification (RCA)

Firstly, linear ssDNA template (1 μM), ligation strand (1 μM) and NaCl (150 mM) were mixed in 100 μL 1× TE buffer (10 mM Tris, 1 mM EDTA, pH 8.0). After hybridization, 20 μL of 10× T4 DNA ligase buffer, 76 μL of water and 4 μL of T4 DNA ligase (5 U/μL, Thermo Fisher Scientific, EL0011) were introduced into the tube for 3 h at room temperature and then rapidly heated to 70 °C for 20 min to inactivate the T4 DNA ligase. Afterwards, 10 μL of Exonuclease I (20 U/μL, Thermo Fisher Scientific, EN0581) and 5 μL of Exonuclease III (200 U/μL, Thermo Fisher Scientific, EN0191) were added to the solution and incubated overnight at 37 °C to remove unhybridized ligation strands and non-circularized templates. The mixture was then heated at 80 °C for 40 min to inactivate the two exonucleases. The circular templates were purified using 10 kDa Amicon Ultra Centrifugal Filters and washed three times with TE buffer.

Secondly, 5 μL of the circularized template (1 μM) was mixed with 67 μL of ultrapure water, 1 μL of primer (10 μM), 10 μL of 10× polymerase buffer, 2 μL of Φ29 DNA polymerase (10 U/μL, Lucigen), 10 μL of inorganic pyrophosphatase (0.1 U/μL, New England Biolabs, M0361L) and 5 μL of adjusted dNTP (100 mM, Thermo Fisher Scientific) mixture. The sample was gently shaken at 30 °C for 60 h and heat-induced cleavage at 95 °C for 15 min. The product was then purified using 30 kDa Amicon Ultra Centrifugal Filters and washed three times with 1× TE buffer. The amount and purity of the ssDNA concentration were then measured using a NanoDrop (Thermo Fisher Scientific).

Preparation of artificial cells

To assemble artificial cells, Plasm-DNA (approximal 10 μM) and Surface-DNA (approximal 2.5 μM) were mixed in 1× TE buffer and heated to 95 °C for 15 min for homogenization. Then 50 mM $MgAc_2$ was added to the solution to facile liquid–liquid phase separation. The STARMs were formed by heating the sample to 95 °C for 20 min at a rate of 3 °C/s. After STARMs formation, stoichiometric amounts of the corresponding fluorescent dye-conjugated oligomers (Alexa 488-p*, s*-TAMRA and Cy5-DNAzyme) were added to the STARMs solution and left for 1 h at room temperature to hybridize with STARMs before imaging using confocal laser scanning microscopy (CLSM, Nikon, Eclipse TE2000-E, Japan).

Determination of T_{cp}

The Plasm-DNA or Surface-DNA was diluted to ~5 μM in 1× TE buffer that contained 50 mM $MgAc_2$ (or different concentration of $MgAc_2$). 1 mL of DNA solution was heated at 1 °C/min, and the extinction at 600 nm was recorded every 30 s. The T_{cp} was determined as the onset of extinction increased at 600 nm. Temperature-dependent UV-vis spectra were recorded on Agilent Cary60 spectrophotometer coupled with a Peltier for accurate temperature control.

Photobleaching experiments

The STARMs labeled with Alexa 488-p* and s*-TAMRA oligomers were first imaged using a low intensity on Leica DMi8 with Leica WF FRAP, a 100 × 1.46 NA oil objective. Photobleaching was achieved using 100% intensity on the 488 nm line. Photobleaching (1.5 s) was used for the STARMs to deplete the fluorescence in the region of interest. Images before and after photobleaching were recorded and the microscopy images were operated by LAS X software.

The preparation of Zn^{2+}-STARM or Light-STARM

To endow STARMs with responsiveness to metal ion Zn^{2+}, Zn^{2+}-DNAzyme (12.5 μL, 10 μM) was added to a freshly prepared STARMs solution (50 μL) to functionalize the surface of STARMs. The DNAzyme-functionalized STARMs (Zn^{2+}-STARM) were left for 2 h at room temperature. The Zn^{2+}-STARM were centrifuged (10,000 × *g*, 5 min) and redispersed with TE buffer containing 50 mM Mg^{2+}. The purified Zn^{2+}-STARM solution was used for further experiments.

To construct STARMs with light responsiveness, we used 10 μM Plasm-DNA, 2.5 μM Surface-DNA, and 1 nM of T_{20}-AuNRs to form Light-STARM following the standard STARM formation method. That is, homogenization for 15 min at 95 °C in TE buffer, followed by the addition of 50 mM $MgAc_2$ and heating to 95 °C for 5 min. The corresponding Light-STARM are displayed in Fig. 5b.

Fluorescence kinetic analysis of Zn^{2+}-STARM surface

To evaluate the ion responsiveness of Zn^{2+}-STARM, we used a fluorophore-quencher system composed of BHQ2-conjugated Zn^{2+} DNAzyme and TAMRA fluorophore-probe that tags the Surface-DNA. The real-time fluorescent of Zn^{2+}-STARM treated with Zn^{2+} (1 mM), Mn^{2+} (1 mM) or Ca^{2+} (1 mM) was monitored by a Synergy™ Mx multi-mode microplate reader (BioTek, USA).

Adhesion evaluation of STARM

Recombinant human MET/HGFR protein (200 nM, 100 μL, Sino Biological, 10692-H27H-B) was added into each well of a 96-well plate (Sigma-Aldrich, S2577) and the plate was incubated overnight at 4 °C. Then, the plate was washed three times with 200 μL of PBS. The Zn^{2+}-STARM-Apt^{MET}/Light-STARM-Apt^{MET} (100 μL) labeled with Alexa 488-p1* oligomers were added to each well and treated with Zn^{2+} (1 mM) or NIR (1 W/cm^2) at different times. Subsequently, the 96-well plate was incubated for 30 min at 37 °C to ensure the combination of STARMs and c-MET/HGFR protein. After washing three times with PBS, the 96-well plate was imaged on Leica DMi8 to monitor the adhesion of STARM cells on the MET-functionalized interface.

Photothermal performance in vitro

1 mL of Light-STARM was irradiated by a fiber-coupled continuous semiconductor diode laser (808 nm, Liangli Optoelectronics Co., Ltd, Changchun, China) with a power density of 1.00 W/cm^2. The temperature of the solutions was measured and recorded one time per 30 s.

Cell culture

All cells were cultured in 5% CO_2 in an incubator at 37 °C. A549 (ATCC, CCL-185), CEM (ATCC, CCL-119), Ramos (ATCC, CRL-1596) cells were cultured in RPMI1640 (Gibico, 11875119) medium supplemented with 10% fetal bovine serum (Biological Industries, 04-001-A) and 1% penicillin and streptomycin (NCM Biotech, C125C5). NIH3T3 (ATCC, CRL-1658) cells were cultured in DMEM (Gibico, 11965092) with 10% super newborn calf serum (Sangon Biotech, E510004) and 1% penicillin and streptomycin.

Confocal laser scanning microscopy (CLSM) imaging

To evaluate the binding ability of Plasm-DNA to mammalian cells, the A549 or NIH3T3 cells were seeded at 35 mm confocal dish in complete medium for 24 h incubation at 5% CO_2 and 37 °C. The A549 or NIH3T3 cells were washed with buffer and then incubated with Plasm-DNA (200 nM) in PBS buffer (100 μL) at 37 °C for 10 min. CEM and Ramos cells (1×10^5) were separately suspended in 200 μL of binding buffer (washing buffer containing yeast tRNA (0.1 mg/mL) and BSA (1 mg/mL)) and then incubated with Plasm-DNA (200 nM) at 4 °C for 30 min. After washing three times with 200 μL of washing buffer (Dulbecco's PBS containing 4.5 g/L glucose and 5 mM $MgCl_2$), the cells were under a confocal laser scanning microscope (CLSM) (Nikon Ti-E, Japan) with a 60× oil immersion objective (Olympus, Melville, NY). The setup of excitation/emission wavelengths for fluorescent imaging was followed the manuals of the fluorescent dyes.

Flow cytometry assay

Flow cytometry was used to evaluate the Plasm-DNA-induced fluorescent shift of cells. Briefly, cells were firstly harvested in cell dissociation buffer to prepare cell suspensions. A549 and NIH3T3 cells (10^5) were incubated with Plasm-DNA (200 nM) in 200 μL PBS buffer at 37 °C for 30 min. 1×10^5 of CEM and Ramos cells were incubated with Plasm-DNA (200 nM) in 200 μL binding buffer at 4 °C for 30 min. After washing three times with 200 μL of washing buffer, the cells were suspended in buffer (200 μL) before flow cytometry analysis using the CytoFLEX flow cytometry (Beckman). Data were processed by FlowJo_V10 software.

Contact-dependent communication between STARM and mammalian cells

The A549 and NIH3T3 cells were seeded at 35 mm confocal dish in complete medium for 24 h incubation at 5% CO_2 and 37 °C. The A549 cells were first incubated with a membrane indicator dye (DiD, Thermo Fisher) in fresh 1640 medium for 15 min. After washing 3 times with 1× PBS, the cells were stimulated with Zn^{2+}-STARM treated with or without Zn^{2+} (1 mM) for 12 h, or the cells incubated with Light-STARM treated with or without NIR laser (1 W/cm^2) for 1 min. Subsequently, the cells were further incubated at 37 °C for 15 min. Finally, cells were washed three times and the cell images were collected with CLSM, and data were analyzed with an ImageJ software.

Preparation of cell lysates and western blot assay

Cells were seeded in a 6-well plate (NEST Biotechnology) until 80% confluence. After the starvation for 24 h in 1640 supplemented with 0.2 % FBS, the medium was changed and stimulated with different

Plasm-DNA or STARM treatment for 10 min. The dishes were put on the ice to stop the stimulation and washed twice with PBS, then lysed with lysis buffer (RIPA buffer with 1% phosphatase inhibitors and protease inhibitor). The cell lysates were centrifuged at 14,000 × *g* for 10 min and the supernatants were retained and saved at −20 °C before use. The cell lysates were separated by 8% SDS-PAGE electrophoresis, then transferred to nitrocellulose membrane by semi-dry electrophoretic transfer unit for 12 min. After blocking with 5% milk-PBST (1× PBS with 0.1% Tween-20) solution for 1 h, the membrane reacted with primary antibody (1:1000 dilution) overnight in 4 °C and IRDye secondary antibody (1:10,000 dilution) for 1 h at room temperature. The primary antibody for phospho-MET (Y1234/5, #3077), phospho-AKT (S473, #4060), phospho-ERK1/2 (T202/Y204, #4370) was obtained from Cell Signaling Technology. The α-tubulin primary antibody was purchased from Cellway Biotechnology Co., Ltd. The IRDye® 800CW Goat anti-Rabbit IgG Secondary Antibody (LI-COR P/N 926-32211), IRDye® 680RD Goat anti-Mouse IgG Secondary Antibody (LI-COR P/N 926-68070) were obtained from LI-COR (Lincoln, Nebraska, USA). All antibodies mentioned above were diluted in universal antibody diluent from New Cell & Molecular Biotech (Suzhou, China). Finally, the fluorescence images were obtained using the LI-COR Odyssey® Infrared Imaging System (Lincoln, Nebraska, USA).

Construction of multicellular assembly

To distinguish three batches of cells in the mixed population, CEM and Ramos cells were labeled with a nuclear fluorescence dye (hoechst, blue fluorescent, Beyotime) and a cytosolic fluorescence dye (DiI, yellow fluorescent, Beyotime), respectively. The Zn^{2+}-STARM-Apt^{Sgc8} and Zn^{2+}-STARM-Apt^{TD05} were labeled with Alexa 488-p1* oligomers (green fluorescence) and Cy5-p2* (red fluorescence), respectively. CCRF-CEM cells were mixed with Ramos cells at a 1:1 ratio (final cell density of 500,000 cells/mL). Then, the mixed cellular system was treated with both Zn^{2+}-STARM-Apt^{Sgc8} and Zn^{2+}-STARM-Apt^{TD05} under $ZnCl_2$ (1 mM) stimulation and gentle shaking for 1 h at 25 °C. Finally, the images of multicellular assembly were observed by confocal laser scanning microscope.

To further verify multicellular assembly, CEM and Ramos cells were labeled with a fluorescent membrane tracer (DiO, green fluorescence, Thermo Fisher) and a fluorescence membrane tracer (DiD, red fluorescence, Thermo Fisher), respectively. After washing with pre-cooled washing buffer three times to remove the unstained solution, CCRF-CEM and Ramos cells mixture was treated with both Zn^{2+}-STARM-Apt^{Sgc8} and Zn^{2+}-STARM-Apt^{TD05} under $ZnCl_2$ (1 mM) stimulation and gentle shaking for 1 h at 25 °C. The cell samples were analyzed with the CytoFLEX flow cytometry (Beckman). Data were processed by FlowJo_V10 software.

ERK response

To visualize the ERK response, A549 cells were transfected with the ERK-kinase translocation reporter (Addgene, 59138) using Lipo8000™ (Beyotime, C0533) transfection reagent based on standard protocols provided by Beyotime. Briefly, cells were seeded on a 35 mm confocal dish and cultured in a complete medium overnight. Subsequently, 100 ng of plasmids mixed with 0.2 μL of Lipo8000™ in Opti-MEM Medium were added for each well, and cells were incubated for at least 24 h. Afterward, the cells were washed twice with PBS and stimulated with Light-STARM-Apt^{MET} treated with or without NIR laser (1 W/cm^2) for 1 min. Then, the cells were incubated at 37 °C for 0, 5, 10, 15, 25 min. The cell images were collected at 488 and 561 nm with a confocal laser scanning system (Nikon Ti-E, Confocal Head A1 MP, Tokyo, Japan) using a 60× oil immersion objective. All fluorescent images were processed, analyzed, and quantified using the ImageJ software.

Cell proliferation assay

The A549 or NIH3T3 (1.0×10^3 cells) were seeded in a 96-well plate (NEST Biotechnology) for 12 h. Then, the medium was removed, and the cells were stimulated with Zn^{2+}-STARM-Apt^{MET} and Light-STARM-Apt^{FGFR1} treated with Zn^{2+} (1 mM) for 12 h or NIR laser (1 W/cm^2) for 1 min. Next, the cells were incubated under 5% CO_2 in a humidified incubator at 37 °C. After 24 h, the proliferation was evaluated using CCK-8 according to the manufacturer's instruction. The data were expressed as the relative values compared with the absorbance (450 nm) of vehicle control.

Dual-channel circuit in co-cultured system

To achieve STARM-cell circuit operating two-channel communication in a multicell system, the cell co-cultivation assay was implemented by the Culture-Insert 2 Well in an ibidi μ-Dish 35 mm. Firstly, 70 μL A549 or NIH3T3 cells were seeded into the Culture-Insert 2 well of the μ-dish co-cultivation system. After cell attachment and confluent in each well, the Culture-Insert was removed, and the co-cultivation system was used for further experiments

Dual-channel circuit for STARM-cell contact evaluation

The A549 and NIH3T3 cells were washed twice with PBS and stimulated with Zn^{2+}-STARM-Apt^{MET} (labeled Alexa 488-p1*, green fluorescence) and Light-STARM-Apt^{FGFR1} (labeled Cy5-p2*, red fluorescence) treated with Zn^{2+} (1 mM) for 12 h or NIR laser (1 W/cm^2) for 1 min. Then, the co-cultured STARM and cells were incubated for 10 min in the incubator. After washing three times with PBS, the cell images were collected with a confocal laser scanning system using a 60× oil immersion objective. All fluorescent images were processed, analyzed, and quantified using the ImageJ software.

In situ immunofluorescence for signal activation by the dual-channel circuit

The co-cultured cells were starved for 24 h in 1640/DMEM supplemented with 0.2% FBS. After the starvation, the medium was changed and stimulated with Zn^{2+}-STARM-Apt^{MET} and Light-STARM-Apt^{FGFR1} treated with Zn^{2+} (1 mM) for 12 h or NIR laser (1 W/cm^2) for 1 min. Then, the co-cultured STARM and cells were incubated for 10 min in the incubator. The media was then removed, and immediately fixed cells by addition of 200 μL of 4% formaldehyde and incubated at 37 °C for 20 min with no shaking. Next, the cells were permeated for 0.5 h in 0.1% TritonX-100 and were blocked for 1 h in 10% goat serum at room temperature with moderate shaking. After that, 200 μL of the desired primary antibody (1:250, phospho-AKT (S473, Cell Signaling Technology, #4060), phospho-ERK (T202/Y204, Cell Signaling Technology, #4370)) was added to the wells and incubated overnight at 4 °C. Washed the μ-dish 5 times with 0.1% tween-20 washing solution for 5 min at room temperature. Next, 1 mL of the secondary antibody (1:2000, IRDye® 800CW Goat anti-Rabbit IgG Secondary Antibody (LI-COR P/N 926-32211)) solution was added and incubated away from light for 60 min with gentle shaking at room temperature. The μ-dish was further washed five times with 0.1% Tween-20 washing solution for 5 min. Finally, clean the bottom dish surface and the images were acquired on the LI-COR Odyssey® Infrared Imaging System (Lincoln, Nebraska, USA).

Single-cell ERK response evaluation by dual-channel circuit

The A549 and NIH3T3 cells were transfected with the ERK-kinase translocation reporter using Lipo8000™ transfection reagent based on standard protocols provided by Beyotime. Afterward, the cells were washed twice with PBS and stimulated with Zn^{2+}-STARM-Apt^{MET} (labeled TAMRA-p1*, yellow fluorescence) and Light-STARM-Apt^{FGFR1} (labeled Cy5-p2*, red fluorescence) treated with Zn^{2+} (1 mM) for 12 h or NIR laser (1 W/cm^2) for 1 min. Then, the co-cultured STARM and cells

were incubated for 10 min in the incubator. After washing three times with PBS, the cell images were collected with a confocal laser scanning system using a 60× oil immersion objective. All fluorescent images were processed, analyzed, and quantified using the ImageJ software.

Characterization of size-gated permeability of STARM

To evaluate the porosity and diffusivity of STARMs, fluorescent proteins of different molecular weights (EGFP, mCherry-DCV, and CBD-mCherry-DCV) were used to analyze the interactions between STARMs and proteins. The Cy5-labeled STARMs were incubated with fluorescent proteins (1 μM) at 37 °C for 10 min. The images were collected with CLSM, and data were analyzed with ImageJ software. The 3D structures of the proteins were generated using AlphaFold 3 (https://alphafold.com/).

Serum stability assessment

The Zn^{2+}-STARM-Apt^{MET} was incubated with 10% FBS for durations of 0, 1, 3, 6, 12 or 24 h at 37 °C, and then thioflavin T (1 μM, THT, Sigma-Aldrich) was adding into Zn^{2+}-STARM-Apt^{MET} in Tris-HCl buffer (pH 7.4, 25 mM Tris, 100 mM KCl) for imaging with CLSM. As for the stability of STARM after ion activation, the Zn^{2+}-STARM-Apt^{MET} was activated by Zn^{2+} (1 mM) for 12 h, then incubated with 10% FBS at 37 °C for 12 h and characterized by confocal imaging using THT.

Cytotoxicity of laser

The A549 cells were cultured for 12 h in a 96-well plate, and then the medium was replaced with fresh medium alone and irradiated with different lengths of time. After washing twice with PBS, CCK-8 assay reagent was added to each well according to the manufacturer's instructions. After 1–4 h in culture, the cell viability was determined by measuring the absorbance at 450 nm using a microplate reader.

Animal studies

All research complied with the relevant ethical regulations. The animal experiments were reviewed and approved by the Animal Ethics Committee of Hunan University (HNUBIO202102004) and the Laboratory Animal Center of Hunan [SYXK (Xiang) 2018-0006]. Adult female Mus musculus (C57BL/6J strain, 7 weeks old) were purchased from Hunan SJA Laboratory Animal Co., Ltd, were housed in viral- and pathogen-free conditions. The mice were housed under controlled conditions at a temperature of 25 ± 2 °C, relative humidity of 45–55%, and a 12-h light/dark cycle. A maximum of 4 animals were housed together and were provided with food and water ad libitum. In order to study the application of STARM in skeletal muscle tissue repair, we used the cardiotoxin (CTX) induced muscle damage in the Tibialis Anterior (TA) muscle. The Light-STARM-Apt^{FGFR1} was injected in situ into the injured site to investigate the tissue repair under NIR light and non-illumination.

For in vivo fluorescence studies, Cy5-labeled Light-STARM-Apt^{FGFR1} were intramuscularly injected into the TA muscle. Then the mice were sacrificed at the designed time points (0, 6, 12, 24, 48, and 72 h), and ex vivo fluorescence of legs and the major organs was recorded using the PerkinElmer IVIS Spectrum CT. The blood samples were collected immediately and the fluorescence intensity of Cy5 in the blood was measured by a Synergy™ Mx multi-mode microplate reader (BioTek, USA).

Cardiotoxin intramuscular injection induced acute skeletal muscle injury model

To induce muscle injury, 50 μL of 20 μM cardiotoxin (CTX, Sigma-Aldrich) was injected intramuscularly into the tibialis anterior (TA) muscle in the left leg using a 29G 1/2 insulin syringe. Non-injured right muscles were injected with PBS as an intact control. After 3 days of continuous CTX injections, the Light-STARM-Apt^{FGFR1} (50 μL) was injected into the injured site in situ and the injured site was irradiated for 3 min at 1.00 W/cm^2. The treatment was repeated for 3 days. The animals were maintained in individual cages with food and water and in a temperature- and humidity-controlled environment. At the end of the study, animals were sacrificed by cervical dislocation.

Immunohistochemistry and histopathology evaluation

Animals were sacrificed 0.5 h or 3 days later, and the muscles were removed, embedded in 4% paraformaldehyde for 24 h, and then the tissue was dehydrated in a sucrose solution for 48 h and embedded in OCT, and 7 μm sections were prepared using in a freezing microtome (Leica, CM1850, Germany). Next, the sections were circled through the immunohistochemical pen, were permeated for 0.5 h in 0.2% TritonX-100 and were blocked for 1 h in 10% goat serum at room temperature. Then, the sections were incubated overnight at 4 °C with primary antibodies phospho-FGFR1 (1:200, Cell Signaling Technology, Tyr653/Tyr654, 52928) Pax7 (1:200, R&D Systems, MAB1675), Ki67 (1:200, Proteintech, 27309-1-AP), Myod (1:200, Santa Cruz Biotechnology, sc-377460) and Myog (1:200, Santa Cruz Biotechnology, sc-12732). Finally, the samples were stained with secondary antibody of Alexa Fluor 488-conjugated Goat anti-mouse IgG, Alexa Fluor 555-conjugated Goat anti-rabbit IgG and Alexa Fluor 555-conjugated Goat anti-mouse IgG (1:200, Sangon Biotech) for 1 h at room temperature, and then stained with DAPI (Solarbio, ID2250) for 5 min. For histopathology evaluation, the samples were prepared with hematoxylin and eosin (H&E) staining for observation. Images were acquired on a Digital slice scanning system (Pannoramic MIDI, 3DHISTECH, Hungary).

Statistics and reproducibility

All data in graphs were presented as means ± standard deviation (s.d.) from at least three biologically independent experiments. All micrograph data were representative of at least three biologically independent experiments with similar results. All statistical significance was determined by unpaired two-tailed Student's *t*-test. n.s. not significant, $^*P < 0.05$, $^{**}P < 0.001$, $^{***}P < 0.001$, and $^{****}P < 0.0001$.

Reporting summary

Further information on research design is available in the Nature Portfolio Reporting Summary linked to this article.

Data availability

All data supporting the findings in this study are provided in the main article, Supplementary Information or Source Data file. Source data is available for Figs. 2, 3, 5, 6 and 7 and Supplementary Figs. 2, 3, 8, 9, 10, 11, 12, 13, 15, 16, 19, 21, 23, 25, 26, 28, 29, 30, 31, 33, 34, 35, 37, 38 and 40 in the associated source data file. Source data are provided with this paper.

References

1. Szostak, J. W., Bartel, D. P. & Luisi, P. L. Synthesizing life. *Nature* **409**, 387–390 (2001).
2. Grzybowski, B. A. & Huck, W. T. S. The nanotechnology of life-inspired systems. *Nat. Nanotechnol.* **11**, 585–592 (2016).
3. Jiang, W. et al. Artificial cells: past, present and future. *ACS Nano* **16**, 15705–15733 (2022).
4. Buddingh, B. C. & Van Hest, J. C. M. Artificial cells: synthetic compartments with life-like functionality and adaptivity. *Acc. Chem. Res.* **50**, 769–777 (2017).
5. Guindani, C., Da Silva, L. C., Cao, S., Ivanov, T. & Landfester, K. Synthetic cells: from simple bio-inspired modules to sophisticated integrated systems. *Angew. Chem. Int. Ed.* **61**, e202110855 (2022).
6. Merindol, R. & Walther, A. Materials learning from life: concepts for active, adaptive and autonomous molecular systems. *Chem. Soc. Rev.* **46**, 5588–5619 (2017).
7. Dzieciol, A. J. & Mann, S. Designs for life: protocell models in the laboratory. *Chem. Soc. Rev.* **41**, 79–85 (2012).

8. Lai, Y.-C. & Chen, I. A. Protocells. *Curr. Biol.* **30**, R482–R485 (2020).
9. Mukwaya, V., Mann, S. & Dou, H. Chemical communication at the synthetic cell/living cell interface. *Commun. Chem.* **4**, 161 (2021).
10. Liu, S. et al. Enzyme-mediated nitric oxide production in vasoactive erythrocyte membrane-enclosed coacervate protocells. *Nat. Chem.* **12**, 1165–1173 (2020).
11. Chen, Z. et al. Synthetic beta cells for fusion-mediated dynamic insulin secretion. *Nat. Chem. Biol.* **14**, 86–93 (2018).
12. Lentini, R. et al. Two-way chemical communication between artificial and natural cells. *ACS Cent. Sci.* **3**, 117–123 (2017).
13. Toparlak, Ö. D. et al. Artificial cells drive neural differentiation. *Sci. Adv.* **6**, eabb4920 (2020).
14. Qian, X., Westensee, I. N., Fernandes, C. C. & Städler, B. Enzyme mimic facilitated artificial cell to mammalian cell signal transfer. *Angew. Chem. Int. Ed.* **60**, 18704–18711 (2021).
15. Adir, O. et al. Synthetic cells with self-activating optogenetic proteins communicate with natural cells. *Nat. Commun.* **13**, 2328 (2022).
16. Bechtel, T. J., Reyes-Robles, T., Fadeyi, O. O. & Oslund, R. C. Strategies for monitoring cell–cell interactions. *Nat. Chem. Biol.* **17**, 641–652 (2021).
17. Belardi, B., Son, S., Felce, J. H., Dustin, M. L. & Fletcher, D. A. Cell–cell interfaces as specialized compartments directing cell function. *Nat. Rev. Mol. Cell Biol.* **21**, 750–764 (2020).
18. Armingol, E., Officer, A., Harismendy, O. & Lewis, N. E. Deciphering cell–cell interactions and communication from gene expression. *Nat. Rev. Genet.* **22**, 71–88 (2021).
19. Kojima, R. & Fussenegger, M. Synthetic biology: engineering mammalian cells to control cell-to-cell communication at will. *ChemBioChem* **20**, 994–1002 (2019).
20. Dekoninck, S. & Blanpain, C. Stem cell dynamics, migration and plasticity during wound healing. *Nat. Cell Biol.* **21**, 18–24 (2019).
21. Scherlinger, M., Richez, C., Tsokos, G. C., Boilard, E. & Blanco, P. The role of platelets in immune-mediated inflammatory diseases. *Nat. Rev. Immunol.* **23**, 495–510 (2023).
22. Friedl, P., den Boer, A., Th & Gunzer, M. Tuning immune responses: diversity and adaptation of the immunological synapse. *Nat. Rev. Immunol.* **5**, 532–545 (2005).
23. Morsut, L. et al. Engineering customized cell sensing and response behaviors using synthetic notch receptors. *Cell* **164**, 780–791 (2016).
24. Huang, X. et al. DNA scaffolds enable efficient and tunable functionalization of biomaterials for immune cell modulation. *Nat. Nanotechnol.* **16**, 214–223 (2021).
25. Garibyan, M. et al. Engineering programmable material-to-cell pathways via synthetic notch receptors to spatially control differentiation in multicellular constructs. *Nat. Commun.* **15**, 5891 (2024).
26. Samanta, A., Baranda Pellejero, L., Masukawa, M. & Walther, A. DNA-empowered synthetic cells as minimalistic life forms. *Nat. Rev. Chem.* **8**, 454–470 (2024).
27. Seeman, N. C. & Sleiman, H. F. DNA nanotechnology. *Nat. Rev. Mater.* **3**, 17068 (2017).
28. Jones, M. R., Seeman, N. C. & Mirkin, C. A. Programmable materials and the nature of the DNA bond. *Science* **347**, 1260901 (2015).
29. Madsen, M. & Gothelf, K. V. Chemistries for DNA nanotechnology. *Chem. Rev.* **119**, 6384–6458 (2019).
30. Bujold, K. E., Lacroix, A. & Sleiman, H. F. DNA nanostructures at the interface with biology. *Chem* **4**, 495–521 (2018).
31. Rothemund, P. W. K. Folding DNA to create nanoscale shapes and patterns. *Nature* **440**, 297–302 (2006).
32. Ke, Y., Ong, L. L., Shih, W. M. & Yin, P. Three-dimensional structures self-assembled from DNA bricks. *Science* **338**, 1177–1183 (2012).
33. Merindol, R., Loescher, S., Samanta, A. & Walther, A. Pathway-controlled formation of mesostructured all-DNA colloids and superstructures. *Nat. Nanotechnol.* **13**, 730–738 (2018).
34. Shi, P., Zhao, N., Coyne, J. & Wang, Y. DNA-templated synthesis of biomimetic cell wall for nanoencapsulation and protection of mammalian cells. *Nat. Commun.* **10**, 2223 (2019).
35. Wang, M. et al. Spatially reprogramed receptor organization to switch cell behavior using a DNA origami-templated aptamer nanoarray. *Nano Lett.* **22**, 8445–8454 (2022).
36. Lu, Y. & Liu, J. Functional DNA nanotechnology: emerging applications of DNAzymes and aptamers. *Curr. Opin. Biotechnol.* **17**, 580–588 (2006).
37. Xiao, M. et al. Assembly pathway selection with DNA reaction circuits for programming multiple cell–cell interactions. *J. Am. Chem. Soc.* **143**, 3448–3454 (2021).
38. Qian, R.-C. et al. Cell surface engineering using DNAzymes: metal ion mediated control of cell–cell interactions. *J. Am. Chem. Soc.* **143**, 5737–5744 (2021).
39. Shi, P. & Wang, Y. Synthetic DNA for cell-surface engineering. *Angew. Chem. Int. Ed.* **60**, 11580–11591 (2021).
40. Joesaar, A. et al. DNA-based communication in populations of synthetic protocells. *Nat. Nanotechnol.* **14**, 369–378 (2019).
41. Chen, H. et al. DNA-based artificial receptors as transmembrane signal transduction systems for protocellular communication. *Angew. Chem. Int. Ed.* **62**, e202301559 (2023).
42. Li, H. et al. A DNA molecular robot that autonomously walks on the cell membrane to drive cell motility. *Angew. Chem. Int. Ed.* **60**, 26087–26095 (2021).
43. Sato, Y., Sakamoto, T. & Takinoue, M. Sequence-based engineering of dynamic functions of micrometer-sized DNA droplets. *Sci. Adv.* **6**, eaba3471 (2020).
44. Samanta, A., Sabatino, V., Ward, T. R. & Walther, A. Functional and morphological adaptation in DNA protocells via signal processing prompted by artificial metalloenzymes. *Nat. Nanotechnol.* **15**, 914–921 (2020).
45. Samanta, A., Hörner, M., Liu, W., Weber, W. & Walther, A. Signal-processing and adaptive prototissue formation in metabolic DNA protocells. *Nat. Commun.* **13**, 3968 (2022).
46. Liu, W., Samanta, A., Deng, J., Akintayo, C. O. & Walther, A. Mechanistic insights into the phase separation behavior and pathway-directed information exchange in all-DNA droplets. *Angew. Chem. Int. Ed.* **61**, e202208951 (2022).
47. Li, C. et al. Leveraging DNA-encoded cell-mimics for environment-adaptive transmembrane channel release-induced cell death. *Angew. Chem. Int. Ed.* **63**, e202406186 (2024).
48. Kambe, T., Taylor, K. M. & Fu, D. Zinc transporters and their functional integration in mammalian cells. *J. Biol. Chem.* **296**, 100320 (2021).
49. Lemmon, M. A. & Schlessinger, J. Cell signaling by receptor tyrosine kinases. *Cell* **141**, 1117–1134 (2010).
50. Boltz, A. et al. Bi-specific aptamers mediating tumor cell lysis. *J. Biol. Chem.* **286**, 21896–21905 (2011).
51. Han, J.-N., Zhong, C., Ge, M., Kuang, S. & Nie, Z. Engineering fluorescent protein chromophores with an internal reference for high-fidelity ratiometric G4 imaging in living cells. *Chem. Sci.* **14**, 4538–4548 (2023).
52. Collinet, C. & Lecuit, T. Programmed and self-organized flow of information during morphogenesis. *Nat. Rev. Mol. Cell Biol.* **22**, 245–265 (2021).
53. Tang, Z. et al. Selection of aptamers for molecular recognition and characterization of cancer cells. *Anal. Chem.* **79**, 4900–4907 (2007).
54. Booth, M. J., Schild, V. R., Graham, A. D., Olof, S. N. & Bayley, H. Light-activated communication in synthetic tissues. *Sci. Adv.* **2**, e1600056 (2016).
55. Deisseroth, K. Optogenetics. *Nat. Methods* **8**, 26–29 (2011).
56. Fernandes, M. et al. MET exon 14 skipping mutation is a hepatocyte growth factor (HGF)-dependent oncogenic driver in vitro and in humanised HGF knock-in mice. *Mol. Oncol.* **17**, 2257–2274 (2023).

57. Kermorgant, S., Zicha, D. & Parker, P. J. PKC controls HGF-dependent c-Met traffic, signalling and cell migration. *EMBO J.* **23**, 3721–3734 (2004).
58. Kudo, T. et al. Live-cell measurements of kinase activity in single cells using translocation reporters. *Nat. Protoc.* **13**, 155–169 (2018).
59. Ma, Y. et al. Synthetic mammalian signaling circuits for robust cell population control. *Cell* **185**, 967–979.e12 (2022).
60. Sockolosky, J. T. et al. Selective targeting of engineered T cells using orthogonal IL-2 cytokine-receptor complexes. *Science* **359**, 1037–1042 (2018).
61. Ueki, R. et al. DNA aptamer assemblies as fibroblast growth factor mimics and their application in stem cell culture. *Chem. Commun.* **55**, 2672–2675 (2019).
62. He, F., Wang, M., Wang, J., Wang, H. & Nie, Z. An extracellular miRNA-responsive artificial receptor via dynamic DNA nano-assembly for biomarker-driven therapy. *Angew. Chem. Int. Ed.* **62**, e202305227 (2023).
63. Xie, Y. et al. FGF/FGFR signaling in health and disease. *Signal Transduct. Target. Ther.* **5**, 181 (2020).
64. Chen, S. et al. Near-infrared deep brain stimulation via upconversion nanoparticle–mediated optogenetics. *Science* **359**, 679–684 (2018).
65. Wang, M. et al. Near-infrared light-activated DNA-agonist nanodevice for nongenetically and remotely controlled cellular signaling and behaviors in live animals. *Nano Lett.* **19**, 2603–2613 (2019).
66. Von Maltzahn, J., Jones, A. E., Parks, R. J. & Rudnicki, M. A. Pax7 is critical for the normal function of satellite cells in adult skeletal muscle. *Proc. Natl Acad. Sci. USA* **110**, 16474–16479 (2013).
67. Berkes, C. A. & Tapscott, S. J. MyoD and the transcriptional control of myogenesis. *Semin. Cell Dev. Biol.* **16**, 585–595 (2005).
68. Zammit, P. S. Function of the myogenic regulatory factors Myf5, MyoD, Myogenin and MRF4 in skeletal muscle, satellite cells and regenerative myogenesis. *Semin. Cell Dev. Biol.* **72**, 19–32 (2017).
69. Stevens, A. J. et al. Programming multicellular assembly with synthetic cell adhesion molecules. *Nature* **614**, 144–152 (2023).

Acknowledgements

This research was supported by the National Key Research and Development Program of China (2024YFA0916700 to N.Z.) and the National Natural Science Foundation of China (22034002 and 92253304 to N.Z., 22177030 to W.H.H.). We thank Ningbo Free Science Technology Co., Ltd. for providing technical assistance on the 3D model of mouse and muscle.

Author contributions

W.M., W.H.H., and N.Z. conceived the presented idea. W.M. carried out the experiments. W.M.X. provided technical assistance for animal-related experiments. W.M., N.H.X., Y.S.H., L.L., W.H.H., and N.Z. analyzed the data. N.Z., W.H.H., and W.M. wrote the manuscript. All the authors discussed the results and commented on the manuscript.

Competing interests

The authors declare no competing interests.

Additional information

Supplementary information The online version contains supplementary material available at https://doi.org/10.1038/s41467-025-57770-1.

Correspondence and requests for materials should be addressed to Hong-Hui Wang or Zhou Nie.

Peer review information *Nature Communications* thanks Dhiraj Bhati and the other, anonymous, reviewers for their contribution to the peer review of this work. A peer review file is available.